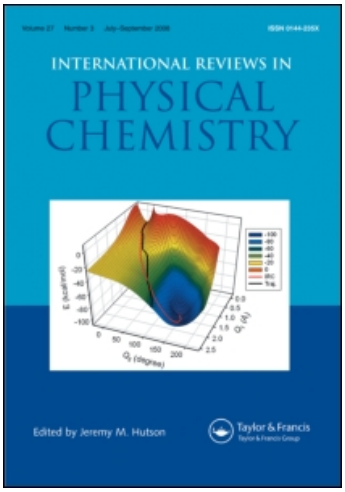

International Reviews in Physical Chemistry
Publication details, including instructions for authors and subscription information:
http://www.informaworld.com/smpp/title~content=t713724383

Classical trajectory simulations of post-transition state dynamics

Upakarasamy Lourderaj[a]; Kyoyeon Park[a]; William L. Hase[a]
[a] Department of Chemistry and Biochemistry, Texas Tech University, Lubbock, Texas 79409

To cite this Article Lourderaj, Upakarasamy , Park, Kyoyeon and Hase, William L.(2008) 'Classical trajectory simulations of post-transition state dynamics', International Reviews in Physical Chemistry, 27: 3, 361 — 403
To link to this Article: DOI: 10.1080/01442350802045446
URL: http://dx.doi.org/10.1080/01442350802045446

International Reviews in Physical Chemistry
Vol. 27, No. 3, July–September 2008, 361–403

Taylor & Francis
Taylor & Francis Group

Classical trajectory simulations of post-transition state dynamics

Upakarasamy Lourderaj, Kyoyeon Park and William L. Hase*

Department of Chemistry and Biochemistry, Texas Tech University, Lubbock, Texas 79409

(*Received 5 January 2008; final version received 8 March 2008*)

Classical chemical dynamics simulations of post-transition state dynamics are reviewed. Most of the simulations involve direct dynamics for which the potential energy and gradient are obtained directly from an electronic structure theory. The chemical reaction attributes and chemical systems presented are product energy partitioning for $Cl^- \cdots CH_3Br \rightarrow ClCH_3 + Br^-$ and $C_2H_5F \rightarrow C_2H_4 + HF$ dissociation, non-RRKM dynamics for cyclopropane stereomutation and the $Cl^- \cdots CH_3Cl$ complexes mediating the $Cl^- + CH_3Cl$ S_N2 nucleophilic substitution reaction, and non-IRC dynamics for the $OH^- + CH_3F$ and $F^- + CH_3OOH$ chemical reactions. These studies illustrate the important role of chemical dynamics simulations in understanding atomic-level reaction dynamics and interpreting experiments. They also show that widely used paradigms and model theories for interpreting reaction kinetics and dynamics are often inaccurate and are not applicable.

Keywords: chemical dynamics; unimolecular reaction dynamics; potential energy surfaces; non-RRKM dynamics; non-IRC dynamics

Contents

*Corresponding author. Email: bill.hase@ttu.edu

ISSN 0144–235X print/ISSN 1366–591X online

DOI: 10.1080/01442350802045446
http://www.informaworld.com

1. Introduction

Many chemical reactions have a potential energy surface (PES) with a rate-controlling transition state (TS), whose properties, when inserted into transition state theory (TST), give an accurate reaction rate constant [1]. Exceptions are reactions with extensive recrossing of this TS [2]. Attributes of the chemical reaction, such as branching between different product channels and reaction pathways [3–5] and partitioning of the available energy to reaction products [6–8], are determined by features of the PES after crossing the rate-controlling TS, and not TST. To contemplate the possible complexity of these *post-transition state dynamics* [9], consider standing at a high energy rate-controlling transition state and gazing towards the reaction products and observing a 'rough' multi-dimensional landscape, with multiple potential energy minima, reaction pathways, low energy barriers, etc. connecting the transition state to multiple product channels. Given the range of possible dynamics resulting from the variety of these PES features, there is considerable interest in determining the actual post-transition state dynamics for chemical reactions.

An extensively used model in chemical kinetics is the statistical theory [10], which assumes understanding the actual atomic-level motion on the PES is unnecessary to interpret a reaction's post-transition state dynamics. For this model, potential energy minima, barriers, and different product channels are connected via reaction paths, determined by following intrinsic reaction coordinates (IRCs) [11]. In the gas phase, where energy of the reactive system is conserved, the statistical model uses Rice–Ramsperger–Kassel–Marcus (RRKM) theory [10] to determine the time the system spends in each potential energy minima and the probabilities for transitions between minima and forming products.

For a chemical reaction in solution, or for a macromolecular reaction, the statistical model assumes that a Boltzmann distribution of energy states exists during all stages of the chemical reaction. It is this assumption which allows one to calculate the potential energy of mean force, i.e. free energy along the reaction path [12,13]. TST is then used to calculate the intermediates' unimolecular lifetimes and probabilities of forming products. The RRKM and TST statistical models assume the only post-transition state PES information needed, to calculate product branching ratios and intermediate lifetimes, are properties of IRCs and the potential energy minima and TS stationary points; which connect the minima and reaction products. For the intermediates, trapped in these minima, rapid

intramolecular vibrational energy redistribution (IVR) is assumed [10,14,15], giving rise to statistical intermediates with energy randomized between their vibrational modes.

The statistical model for gas-phase product energy partitioning is phase space theory [16] (PST) or a modified PST, which assumes adiabatic energy levels [17] or couplings between these levels [18] as the reaction products separate. If there is repulsive potential energy release as the reactive system moves directly from the rate-controlling TS to product, statistical theory does not correctly model product energy partitioning [6]. It is often assumed that the statistical model for product energy partitioning becomes applicable if there is a deep potential energy well in the exit channel, as the system moves from the TS to products, and the interaction potential between the products is purely attractive with no potential energy maximum. The assumption is that the potential energy well gives rise to intermediate formation and statistical IVR.

It is important to study the accuracy of the above statistical model for post-transition state dynamics and classical trajectory chemical dynamics simulations [19] may be used to do this. Until recently, the standard approach for performing a trajectory simulation was to represent the PES for a chemical reaction by either an empirical analytic function, with adjustable parameters, or as an analytic function fit in total or in part to *ab initio* potential energies [20]. Since the number of independent coordinates is $3N-6$ for a nonlinear system with N atoms, to fit a PES with potential energies for each internal coordinate at NP different positions, a total of $(NP)^{3N-6}$ *ab initio* points are required. Thus, only for reactive systems with a small number of atoms is it practical to derive the PES completely from *ab initio* calculations. An approach often used for larger polyatomic systems is to derive, from *ab initio* calculations, an analytic potential energy function for the degrees of freedom thought to be most critical for the dynamics, and use empirical analytic potential energy terms for the remaining degrees of freedom [20,21]. This latter empirical potential, similar to the molecular mechanical (MM) model [22], is usually fit to experimental data such as force constants, equilibrium geometries, and bond energies.

The above approaches for representing the PES have limitations. The use of empirical potentials, such as the London–Eyring–Polanyi–Sato (LEPS) function [23], and the exact fitting of the PES to *ab initio* calculations are limited to chemical reactions with very few atoms. Using the mixed *ab initio*/empirical PES model for polyatomic PESs has ambiguities, since there always are uncertainties in identifying which coordinates are critical and must be described accurately. Potential energy coupling terms between the critical and non-critical coordinates are necessarily approximate. Moreover, identifying potential energy functions for the critical coordinates, which represent their potential energies and also smoothly connect with those for the non-critical coordinates, may be a difficult task [20,21]. Accomplishing this, in conjunction with separating critical and non-critical coordinates and fitting the electronic structure calculations, is often a lengthy process.

With increased computer speed and more powerful computer algorithms, it has become possible to perform *direct dynamics simulations* [19,24,25], in which electronic structure theory is used directly without the need for an empirical or analytic potential energy function or having to distinguish between critical and non-critical degrees of freedom. The trajectories are integrated 'on the fly' with the potential energy and its derivatives obtained directly from an electronic structure theory. This was first implemented by Wang and Karplus [26] using semi-empirical electronic structure theory and later *ab initio* theory was applied by Leforestier [27]. The two strengths of direct

dynamics are that it gives the time-dependent 'unadulterated' classical trajectories for a particular electronic structure theory, concomitant with time-independent properties such as structures, frequencies, energies, etc. and, in avoiding the necessity of developing an analytic potential energy function, it opens up applications of chemical dynamics simulations to a broad spectrum of chemical reactions. As a result of the former, there is no uncertainty in testing different electronic structure theory methods when comparing with experiment. The only limitation for the latter is the technical feasibility of the chemical dynamics application given the computation requirements [19,24,25].

In this review the results of several chemical dynamics simulations, which address post-transition state dynamics, are described. The topics and chemical reactions considered are product energy partitioning for $Cl^- \cdots CH_3Br \rightarrow ClCH_3 + Br^-$ and $C_2H_5F \rightarrow C_2H_4 + HF$ dissociation [28–31], the non-statistical dynamics for trimethylene stereomutation [32–35] and $Cl^- + CH_3Cl$ S_N2 nucleophilic substitution [36–46], and the non-IRC reaction paths for the $OH^- + CH_3F$ [47] and $F^- + CH_3OOH$ [48] reactions. Except for the $Cl^- \cdots CH_3Br \rightarrow ClCH_3 + Br^-$ study [28] and components of the $Cl^- + CH_3Cl$ calculations [36–43], the simulations were performed using direct dynamics.

2. Classical trajectory calculations

2.1. *Direct dynamics simulations*

In a classical chemical dynamics simulation an ensemble of trajectories is calculated, which represents the conditions of the reactants for the chemical reaction under investigation [49,50]. Each trajectory is evaluated by numerically integrating either Hamilton's

$$E = H = T + V \tag{1a}$$

$$\frac{\partial p_i}{\partial t} = -\frac{\partial H}{\partial q_i} \text{ and } \frac{\partial q_i}{\partial t} = \frac{\partial H}{\partial p_i} \tag{1b}$$

or Newtons's

$$-\frac{\partial V}{\partial q_i} = \frac{m_i \partial^2 q_i}{\partial t^2} \tag{2}$$

classical equations of motion. Newton's equations must be integrated in a rectilinear coordinate system (e.g. Cartesian coordinates), while any set of conjugate coordinates and momenta may be used to integrate Hamilton's equations (e.g. curvilinear internal coordinates for which the kinetic energy T depends upon both coordinates and momenta).

For a direct dynamics simulation, the trajectory is integrated using information obtained directly from an electronic structure theory. Two approaches have been advanced for performing direct dynamics simulations [19,24,25]. In Car–Parrinello direct dynamics the electronic wavefunction and nuclear motion are propagated simultaneously, without reoptimization of the wavefunction at each integration step [51]. The wavefunction is propagated using fictitious electronic degrees of freedom. Quite small masses must be used for these degrees of freedom to suppress coupling between the electronic and nuclear degrees of freedom, which may result in unphysical dynamics [52], including artificial electronic transitions [19].

Born–Oppenheimer direct dynamics is used for the simulations reviewed here [19,24]. This method combines traditional classical trajectory simulations [53] and electronic structure theory calculations. At each step of the trajectory integration the potential energy V, gradient $\partial V/\partial q_i$, and also Hessian $\partial^2 V/\partial q_i^2$ for some applications (see below) are obtained directly by solving the time-independent electronic Schrödinger equation. To ensure the accuracy of the simulations, the need for time-reversible trajectories [54,55] and a strict self-consistent-field (SCF) convergence criterion has been stressed [56].

Direct dynamics simulations become computationally quite expensive for a high-level electronic structure theory and it is, thus, important to use the largest numerical integration step size while maintaining the accuracy of the trajectory. For direct dynamics simulations, which only use the gradient, symplectic integrators [19,24,57,58] are fastest [59] and allow one to use the largest integration step size. These integration methods preserve the Poincaré integral invariants that are found in the exact Hamiltonian dynamics and also preserve the volume of phase space [60]. Symplectic methods typically give good energy conservation for long time integrations, using large integration step sizes, and are superior to predictor–corrector non-symplectic schemes that yield a continuous drift in energy [19,24]. The most widely used symplectic integrators are the fourth-order Verlet [61], velocity-Verlet [62], or their derivatives [62]. If more stability is required in the numerical integration, a sixth-order symplectic integrator may be used [63,64].

To use a large integration step, Helgaker *et al.* [65] proposed a scheme that uses the Hessian. If the Hessian is given directly by the electronic structure theory, a local approximation to the true PES can be made using a second-order Taylor expansion and the trajectories can be calculated using this approximate potential; i.e.

$$V(\mathbf{q}) = V_1 + \mathbf{G}_1^T \Delta\mathbf{q} + \frac{1}{2}\Delta\mathbf{q}^T \mathbf{H}_1 \Delta\mathbf{q} \tag{3}$$

where $\Delta\mathbf{q} = \mathbf{q} - \mathbf{q}_1$, and V_1, $\mathbf{G}_1$, and $\mathbf{H}_1$ are the energy, gradient, and Hessian evaluated at $\mathbf{q}_1$. The local quadratic potential is only valid in a small region, called a 'trust region' defined by a trust radius. The equations of motion are integrated to the end of the trust radius, where the potential, gradient, and Hessian are calculated to define a new local quadratic PES for integrating the trajectory. Since the potential, gradient, and Hessian are known at the starting and the ending of each integration step, Millam *et al.* [66] used a fifth-order polynomial to fit the potential between the two points and correct the trajectory. This gives a more accurate trajectory in the trust region and allows one to take large integration steps. The integration on the approximate quadratic model potential is called the 'predictor step' and that on the fifth-order PES is called the 'corrector step'. The computational cost for the Hessian evaluations can be considerably reduced if some are approximated using a Hessian updating scheme, and Bofill's [67] was found to be most suitable [68].

Millam *et al.* [66] performed the predictor integration step in instantaneous normal mode coordinates [69], an approach which does not conserve angular momentum even if the initial total angular momentum is zero [70,71]. In addition, their corrector interpolation and integration were performed in a rotated Cartesian space which does not conserve angular momentum [72], since the local potential expanded in Cartesian coordinates is not rotationally invariant [73]. Angular momentum was conserved by a subsequent numerical treatment of the predicted trajectory [66].

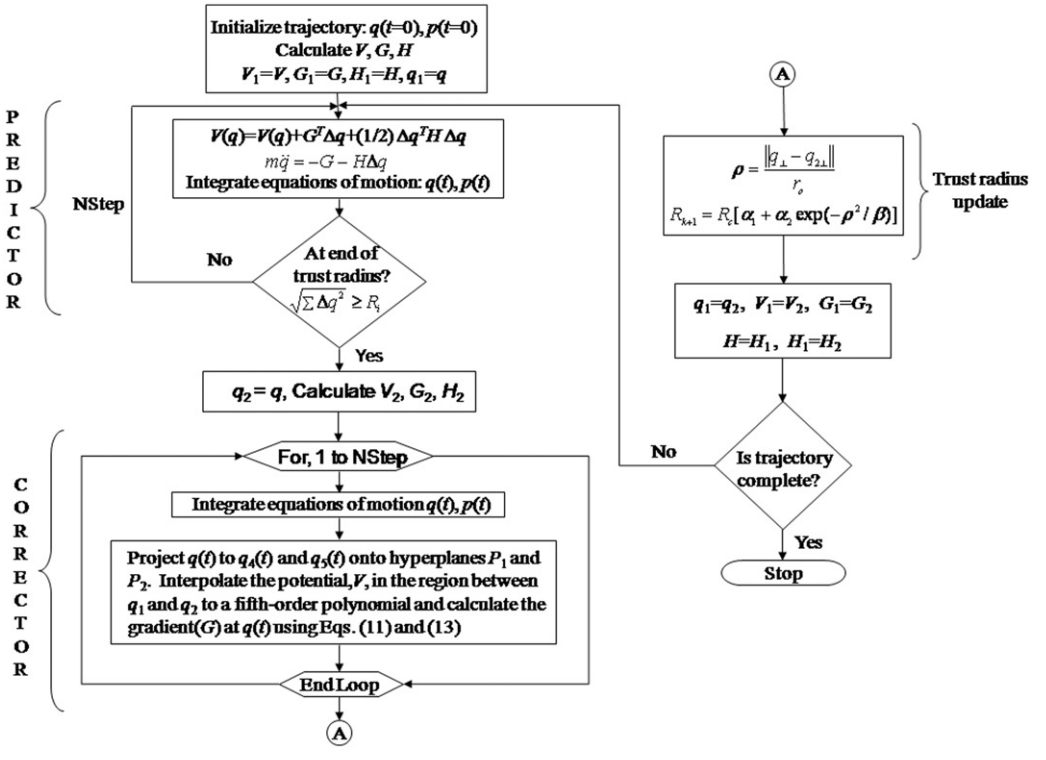

Figure 1. Flowchart representation of the complete Hessian-based integrator. (Reprinted with permission from J. Chem. Phys. 126, 044105. Copyright 2007. American Institute of Physics.)

Improvements to this Hessian-based integration scheme were developed by Lourderaj *et al.* [59] A predictor step using the quadratic potential model is taken to the end of the trust radius using the symplectic velocity-Verlet integration algorithm [62] to integrate Newton's equation in Cartesian coordinates, instead of instantaneous normal mode coordinates. Unrotated Cartesian coordinated are used for the corrector step to assure the constants of motion are conserved. The trust radius for the next step is updated using a new algorithm based on the difference between the predicted and corrected trajectories. This modified Hessian-based integration algorithm, with its new components, was implemented into the VENUS/NWChem [74–76] software package and compared with the velocity-Verlet and Adams–Moulton integration algorithms for the $H_2CO \rightarrow H_2 + CO$, $O_3 + C_3H_6$, and $F^- + CH_3OOH$ chemical reactions [59]. The complete Hessian-based integration algorithm is summarized as a flowchart in Figure 1. Specific details for each component of the flowchart are given in reference [59].

2.2. *Trajectory initial conditions*

To use classical trajectory simulations to compare with experiment it is important to choose molecular systems to study for which classical mechanics is expected to give

accurate results. This is discussed in detail below where quantum effects are reviewed, and where it is pointed out that extensive comparisons of classical dynamics with experiment and/or exact quantum dynamics have illustrated that classical dynamics gives accurate results for direct classically allowed processes, which occur on a short time-scale [10,24,77–80]. Three types of direct processes are considered in this review. One is direct, non-statistical unimolecular dissociation. The second is the dynamics of highly exothermic bimolecular association reactions, with complex post-transition state dynamics after passing the association variational TS. The third is the post-transition state dynamics after passing a rate controlling TS barrier on the PES. The latter may be either a constant energy or constant temperature process.

To compare the results of a classical trajectory simulation with experiment it is important to choose initial conditions for the trajectories which correspond to those of the experiment. The approach is to properly sample the reactants' vibrational and rotational energy levels and this is done by the quasiclassical model, which has been described in detail for unimolecular and bimolecular reactions [50] and is not reviewed here. A less extensively used approach for simulating post-transition state dynamics is to initialize the trajectories at a rate controlling TS and then propagate their dynamics from the TS.

For a constant temperature experiment the transition state theory (TST) rate constant for the rate controlling TS is given by

$$k(T) = \frac{k_B T}{h} \frac{Q^{\ddagger}}{Q} e^{-E_o/k_B T} \tag{4}$$

where $Q^{\ddagger}$ and Q are the partition functions for the TS and reactants, respectively, and E_o is the potential energy difference (including ZPE's) between the TS and reactants. TST assumes the populations of the TS's energy levels are given by their Boltzmann distributions, which forms a canonical ensemble at the TS. The normal mode and rigid rotor model may be used to sample the Boltzmann distribution for each of the TS's vibrational and rotational quantum numbers; i.e. $\boldsymbol{n}$, J, and K for a symmetric top, where $\boldsymbol{n}$ denotes the TS's $3N-7$ vibrational quantum numbers [39,50]. The quasiclassical model is then used to transform these quantum numbers into normal mode coordinates and momenta, and the three-components of the rotational angular momentum. The reaction coordinate translational energy $E_t^{\ddagger}$ is treated classically and selected by sampling its Boltzmann distribution [39,50]

$$P\left(E_t^{\ddagger}\right) = \frac{\exp\left(-E_t^{\ddagger}/k_B T\right)}{k_B T} \tag{5}$$

The reaction coordinate momentum is $P_t^{\ddagger} = 2(E_t^{\ddagger})^{1/2}$. The normal mode coordinates and momenta, the rotational angular momenta, and the reaction coordinate momentum are then transformed into Cartesian coordinates and momenta, and the integration of the trajectory and propagation from the TS to products is initiated.

The above scheme for choosing initial conditions for a rate controlling TS may apply for either a bimolecular or unimolecular reaction. The latter reactions are also often performed at a fixed vibrational energy and well-defined angular momentum so that, if the molecule's unimolecular decomposition dynamics is in accord with the rapid IVR assumption of RRKM theory, there is a microcanonical ensemble of states at the

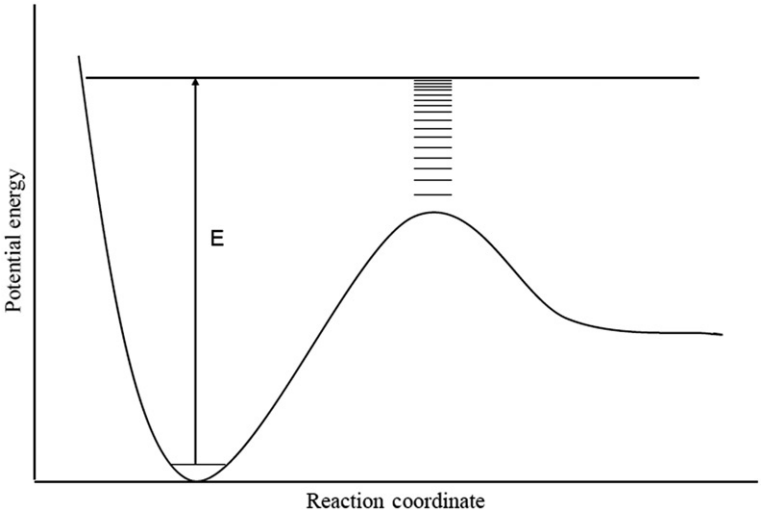

Figure 2. Depiction of vibrational/rotational levels at the transition state for a unimolecular reaction. According to RRKM theory, each level has an equal probability of being populated. (L. Sun and W. L. Hase, in *Review in Computational Chemistry,* Vol. 19, edited by K. Lipkowitz, R. Larter, and T. R. Cundari. Reprinted with permission of John Wiley and Sons. Inc. Copyright 2003.)

decomposition TS. The TS's vibrational/rotational states are depicted in Figure 2 and, for a microcanonical ensemble at the TS, each of the states has an equal probability of being populated [10]. With E, the total energy of the unimolecular reactant, the energy of the TS is $E^{\ddagger} = E - E_o$ and given by

$$E^{\ddagger} = E^{\ddagger}_{nJK} + E^{\ddagger}_{t} \tag{6}$$

for a symmetric top molecule.

A quasiclassical normal mode model [29,50,81] may be used to sample the TS's microcanonical ensemble. The probability that normal mode j at the TS has quantum number $n_j^{\ddagger}$ is

$$P\left(n_j^{\ddagger}\right) = \frac{N\left[E^{\ddagger}_{\mathrm{vt}} - E\left(n_j^{\ddagger}\right)\right]}{N(E^{\ddagger})} \tag{7}$$

where $E^{\ddagger}_{\mathrm{vt}}$ is the vibration and reaction coordinate translation energy of the TS in excess of its ZPE, $N(E^{\ddagger}_{\mathrm{vt}})$ is the TS's total number of states with energy $E^{\ddagger}_{\mathrm{vt}}$, $N[E^{\ddagger}_{\mathrm{vt}} - E(n_j^{\ddagger})]$ is the TS's number of states with $n_j^{\ddagger}$ quanta in mode j, and $E(n_j^{\ddagger}) = (n_j^{\ddagger} + 1/2)h\nu_j^{\ddagger}$. Once $n_j^{\ddagger}$ has been selected, the quantum number for the next mode is selected using the same probability distribution as above, except the energy available to the mode is equal to $E^{\ddagger}_{\mathrm{vt}} - E(n_j^{\ddagger})$. The procedure is then repeated for the remaining modes. The transition state has $s^{\ddagger}$ vibrational modes and, after quantum numbers have been selected for the modes, the energy available for the remaining mode is

$$E^{\ddagger}_{\mathrm{vt}} - \sum_{j=1}^{s^{\ddagger}-1} E\left(n_j^{\ddagger}\right). \tag{8}$$

A state for the remaining mode is chosen randomly within this maximum energy. The energy not assigned to the $s^{\ddagger}$ vibration modes is then added to reaction coordinate translation; i.e.

$$E_t^{\ddagger} = E_{\mathrm{vt}}^{\ddagger} - \sum_{j=1}^{s^{\ddagger}} E\left(n_j^{\ddagger}\right). \tag{9}$$

The Beyer–Swinehart algorithm [82] may be used to determine the numbers of states in Equation (7).

Using this sampling algorithm, each TS vibrational level has equal probability of being populated and the distribution of reaction coordinate translational energy is

$$P\left(E_t^{\ddagger}\right)\mathrm{d}E_t^{\ddagger} = \frac{\rho\left(E_{\mathrm{vt}}^{\ddagger} - E_t^{\ddagger}\right)\mathrm{d}E_t^{\ddagger}}{N\left(E_{\mathrm{vt}}^{\ddagger}\right)}, \tag{10}$$

where $\rho(E_{\mathrm{vt}}^{\ddagger} - E_t^{\ddagger})$ is the density of vibrational states for energy $E_{\mathrm{vt}}^{\ddagger} - E_t^{\ddagger}$. The numerators in Equations (7) and (10) are related by

$$\int_0^{E_t^{\ddagger}} \rho\left(E_{\mathrm{vt}}^{\ddagger} - E_t^{\ddagger}\right)\mathrm{d}E_t^{\ddagger} = \sum_{j=1}^{s^{\ddagger}} \sum_{n=0}^{n_{\max}} N\left[E_{\mathrm{vt}}^{\ddagger} - E_t^{\ddagger} - E\left(n_j^{\ddagger}\right)\right]. \tag{11}$$

The TS's rotational energy is assumed to be adiabatic [83–85].

2.3. *Quantum effects*

The accuracy of classical chemical dynamics simulations and the possible importance of quantum effects have been reviewed in detail [10,24,77,78]. Comparisons of classical chemical dynamics simulations with experiment and quantum dynamics calculations have shown that trajectories give correct results for direct processes such as direct bimolecular reactions, unimolecular fragmentation dynamics on repulsive potential energy curve, short-time unimolecular decomposition and intramolecular vibrational energy flow, and the unimolecular dissociation of small molecules whose intramolecular dynamics is intrinsically RRKM [86]. For these direct processes the unphysical flow and pooling of ZPE [79,80,87] is less important and the classical dynamics tends to maintain the vibrational adiabaticity present in quantum dynamics. However, the trajectories do not describe tunneling and interferences in which multiple classical paths lead to the same quantum state. Electronic non-adiabatic dynamics may be incorporated into the classical chemical dynamics by using a semiclassical model to allow transitions between electronically adiabatic potential energy surfaces [88]. In the following, the agreement between classical and quantum dynamics is described for the types of chemical processes considered in this review.

The dynamics of a highly exothermic bimolecular association reaction, with a variational TS, and the product forming dynamics of a high energy TS are akin to the photodissociation dynamics on a repulsive potential energy curve [89]. Schinke and coworker have shown that the classical and quantum dynamics are similar for the latter [90]. In the work reviewed below, it is shown that classical chemical dynamics simulations,

give results in good agreement with experiment for the branching between product channels for the $F^- + CH_3OOH$ reaction [48] and for $C_2H_5F^{\ddagger} \rightarrow C_2H_4 + HF$ product energy partitioning [31]. Classical dynamics also give accurate product enery partitioning for $C_2H_4F^{\ddagger} \rightarrow C_2H_3F + H$ [72].

If the intramolecular dynamics of a randomly excited molecule is ergodic on the time-scale of its unimolecular dissociation, a microcanonical ensemble of states will be present during all times of its dissociation and its dissociation probability will be exponential with a rate constant $k(E)$ given by classical RRKM theory [10,86]. In contrast, a small molecule dissociates quantum mechanically via isolated resonance states and, if the classical dynamics is ergodic, the classical/quantum correspondence is that these states can not be assigned quantum numbers and the chaotic properties of their wavefunctions ψ_n give rise to statistical fluctuations in their rate constants k_n [10,91,92]. The correspondence found between the classical $k(E)$ and the quantum k_n, for an energy interval ΔE, is that the average of the k_n equals $k(E)$ [78,93,94]. For a small molecule, ZPE constraints become small and the classical and quantum RRKM $k(E)$ are nearly the same.

Agreement between experiment and chemical dynamics simulations is found for $Cl^- \cdots CH_3Cl \rightarrow Cl^- + CH_3Cl$ dissociation. There is very weak coupling between the three low-frequency intermolecular modes (i.e. the $Cl^- \cdots C$ stretch and the degenerate $Cl^- \cdots CH_3$–Cl bends) and the nine CH_3Cl intramolecular modes of the $Cl^- \cdots CH_3Cl$ complex [37,38,42]. $Cl^- + CH_3Cl$ association forms a complex in which only the three intermolecular modes are excited and the unimolecular rate constant for the initial decomposition of this complex is in excellent agreement with experiment [95]. Thus, the dissociation occurs via an 'effectively small molecule' and the agreement between experiment and the classical dynamics is expected from the discussion given above. Both experiments [96] and chemical dynamics simulations [28] show a similar state specificity for dissociation of the $Cl^- \cdots CH_3Br$, in which exciting the intermolecular modes forms $Cl^- + CH_3Br$, while exciting the intramolecular modes forms $ClCH_3 + Br^-$.

3. Product energy partitioning

A relatively uncomplex attribute of post-transition state dynamics is the partitioning of the available energy to the reaction products. Though trajectories are widely used to study the unimolecular dissociation dynamics of highly excited molecules, in general the dissociating trajectories do not give accurate product energy distributions. This is because, in the absence of tunneling, the TS barrier for a unimolecular reaction is the vibrationally adiabatic barrier with ZPE in the degrees of freedom orthogonal to the reaction coordinate. The intramolecular dynamics of many molecules is ergodic on the time-scale of the unimolecular reaction. The molecule's phase space is occupied in accord with a classical microcanonical ensemble and its unimolecular rate constant is that of classical RRKM theory. The classical unimolecular dissociation dynamics for such a molecule do not conform to the quantum TS vibrational adiabaticity and trajectories may cross the barrier with an energy in the modes orthogonal to the reaction coordinate which is less than the ZPE [97]. The classical mechanical barrier for unimolecular dissociation is the classical threshold, which does not include the TS's ZPE.

One approach for using classical trajectories to calculate product energy partitioning distributions, which may be compared with experiment, is to initiate the trajectories at

the TS with initial conditions that correspond to the TS's energy levels sampled by the unimolecular dissociation of the excited molecule [29]. In general the population of the TS's energy levels is not known, but if the unimolecular dissociation of the molecule is in accord with RRKM theory it may be assumed that each TS energy level has an equal probability of being populated, as postulated by RRKM theory (see Figure 2) [10]. Thus, if the transition from the TS to products is a direct process, simulations of photodissociation [90] and unimolecular exit-channel dynamics [29–31] have shown that an ensemble of trajectories properly initiated at the TS will give accurate product energy partitioning distributions. As described above in Section 2.2, for each trajectory one of the $E^{\ddagger}_{nJK}$ energy levels in Equation (6) is randomly selected with the remaining energy placed in reaction coordinate translation. The ensemble of trajectories is then directed towards products to determine the product energy partitioning. In previous work the RRKM assumption of equal population of TS energy levels has been used to calculate product energy partitioning distributions for $C_2H_4F^* \rightarrow C_2H_3F + H$ [72], $H_2CO^* \rightarrow H_2 + CO$ [98], and $C_2H_5F^* \rightarrow C_2H_4 + HF$ [29–31] dissociation and good agreement has been found with experiment.

If the unimolecular dissociation of the molecule is non-statistical and not in accord with RRKM theory, equal population of the TS's energy levels is not expected [9]. For such a simulation it may be possible to vary the population of the TS energy levels in the simulation until the calculated and experimental product energy distributions agree. Such an analysis has not been performed and the uniqueness of the population of the TS energy levels, as specified by the product energy partitioning, is unknown.

Here we review simulations for both $Cl^- \cdots CH_3Br^* \rightarrow ClCH_3 + Br^-$ and $C_2H_5F^* \rightarrow HF + C_2H_4$ dissociation. The intramolecular dynamics of the former is highly non-ergodic and non-RRKM and the trajectories are initiated in the $Cl^- \cdots CH_3Br^*$ complex. Experiments show that the dissociation kinetics of $C_2H_5F^*$ are in accord with RRKM theory and for this simulation the trajectories are initiated at the dissociation TS. The presentation for this latter study also includes a discussion of mass effects and the use of a single trajectory to determine the manner in which the exit-channel potential energy release is partitioned to product energies.

3.1. $Cl^- \cdots CH_3Br^* \rightarrow ClCH_3 + Br^-$

The potential energy surface for gas-phase S_N2 nucleophilic substitution reactions of the type

$$X^- + CH_3Y \rightarrow XCH_3 + Y^- \tag{12}$$

have $X^- \cdots CH_3Y$ and $XCH_3 \cdots Y^-$ pre- and post-reaction potential energy minima (Figure 3). The statistical model for chemical kinetics assumes reaction intermediates are formed in these minima with rapid IVR, so that their intramolecular dynamics is ergodic and their unimolecular rate constants are given by RRKM theory. However, both experiments [96] and chemical dynamics simulations [37,38,41,42] have shown the unimolecular dynamics of these complexes are highly non-statistical with inefficient energy flow between the complexes' intermolecular and intramolecular modes.

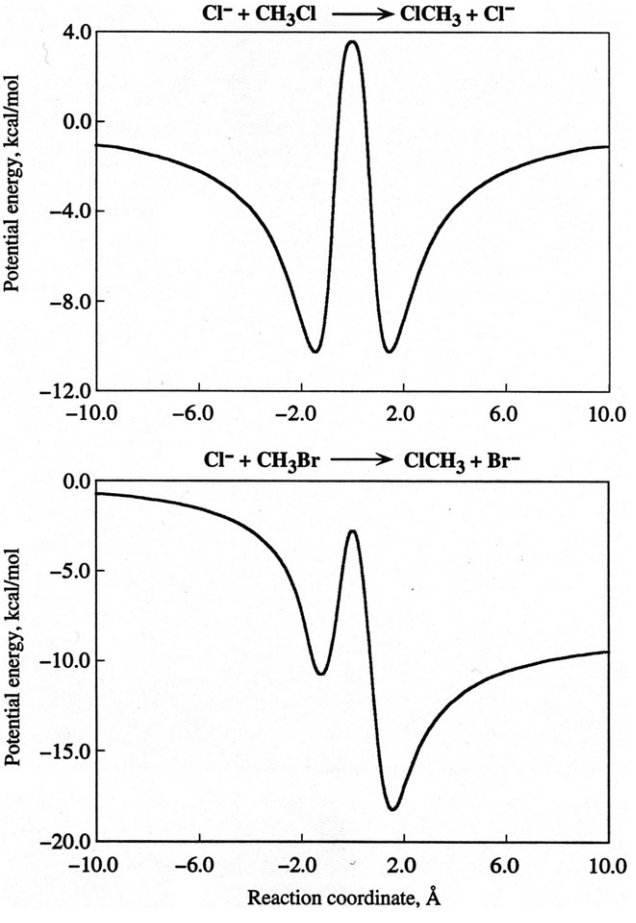

Figure 3. Reaction path potentials for $Cl^- + CH_3Cl \rightarrow ClCH_3 + Cl^-$ and $Cl^- + CH_3Br \rightarrow ClCH_3 + Br^-$ S_N2 nucleophilic substitution [41].

One S_N2 reaction, for which the experimental results are inconsistent with the statistical model, is

$$Cl^- + CH_3Br \rightarrow ClCH_3 + Br^-. \tag{13}$$

The dissociation kinetics of $Cl^- \cdots CH_3Br$ complexes, formed by $Cl^- + CH_3Br$ association, do not simply depend on their total energy as assumed by RRKM theory, but whether their energy is acquired from $Cl^- + CH_3Br$ relative translation or CH_3Br vibration [99–101]. Another way to probe the adequacy of the statistical model for describing the kinetics of reaction (13) is to measure the $ClCH_3 + Br^-$ product energy partitioning. Statistical product energy partitioning is given by orbiting transition state/phase space theory (OTS/PST) [16], which assumes statistical energy partitioning at the orbiting transition state for dissociation of the post-reaction complex $ClCH_3 \cdots Br^-$. In an experimental study of $Cl^- \cdots CH_3Br$ dissociation, Graul and Bowers [102,103] measured

the relative translational energies between the $ClCH_3 + Br^-$ reaction products and found them to be much smaller than the prediction of OTS/PST.

A chemical dynamics simulation was performed [28] to model the experiments of Graul and Bowers, and study the intramolecular and unimolecular dynamics of the $Cl \cdots CH_3Br^-$ complex. An analytic potential energy function, fit in part to *ab initio* calculations as described above in Sections 1 and 2.1, was used for the simulations. This function is thought to give an accurate representation of the reaction's PES, since it accurately describes the rate of reaction (13) versus reagent translational energy [104,105], $Cl^- \cdots CH_3Br$ unimolecular dynamics [28,96], and $ClCH_3 + Br^-$ product energy partitioning (see below) as compared to experiment. The same function, but with different parameters, gives dynamics for the $Cl^- + CH_3Cl$ S_N2 reaction in good agreement with both experiment [95] and direct dynamics simulations [45].

In the chemical dynamics simulations different initial non-random energy distributions were investigated for the $Cl \cdots CH_3Br^-$ complex by exciting, for each simulation, only one of its normal modes with approximately 13.4 kcal/mol above the $Cl \cdots CH_3Br^-$ ZPE level. The total energy available for partitioning to the $ClCH_3 + Br^-$ reaction products is then approximately 15.6 kcal/mol. Two distinct patterns are observed in the dissociation dynamics of the $Cl^- \cdots CH_3Br$ complex. When either one of the three low-frequency intermolecular modes is excited, the complex preferentially dissociates to the $Cl^- + CH_3Br$ reactants. In contrast and in agreement with experiments by the McMahon research group [96], when one of the high-frequency CH_3Br intramolecular modes is excited, the above is a negligible reaction path and, instead, $Cl^- \cdots CH_3Br \rightarrow ClCH_3 \cdots Br^-$ central barrier crossing becomes important. Contrary to RRKM theory, the $ClCH_3 \cdots Br^-$ complexes formed by this isomerization do not immediately dissociate to the $ClCH_3 + Br^-$ products and instead many of the trajectories have extensive recrossings of the central barrier before forming the products. The post-transition state dynamics after crossing the $[Cl \cdots CH_3 \cdots Br]^-$ central barrier is decidedly non-RRKM. Similar central barrier recrossing is found for the $Cl^- + CH_3Cl$ S_N2 reaction (see below) [39,45]. Relative timescales for intramolecular vibrational energy redistribution, $Cl^- \cdots CH_3Br \rightarrow Cl^- + CH_3Br$ dissociation, and $Cl^- \cdots CH_3Br \rightarrow ClCH_3 \cdots Br^-$ isomerization have not been established, since the latter reactions have non-exponential probabilities and multiple rate constants [28,37,42]. Determining meaningful relationships between these rate constants and IVR rate constants is a topic of considerable interest.

A comparison of the trajectory and OTS/PST product energy partitioning shows that OTS/PST predicts a higher average relative translational energy and a lower average vibrational energy than found from the trajectories [28]. However, to compare with the experimental $ClCH_3 + Br^-$ product translational energy distribution, two issues must be considered. The potential energy surface used for the simulations has a reaction exothermicity of 12.3 kcal/mol, while the best experimental estimate of this exothermicity is 8–9 kcal/mol [28]. In addition, the initial excitation energy of the $Cl^- \cdots CH_3Br$ complex is different for the simulation and experimental studies. If the trajectory results are scaled so that the energy available to the products matches that of the experimental study [103], the average product relative translational energy is 0.8 kcal/mol in excellent agreement with the experimental value of 0.7 ± 0.2 kcal/mol, and considerably different than the OTS/PST value of 1.6 kcal mol. The trajectory and OTS/PST product energy distributions are compared in Figure 4, along with the experimental distribution for the relative

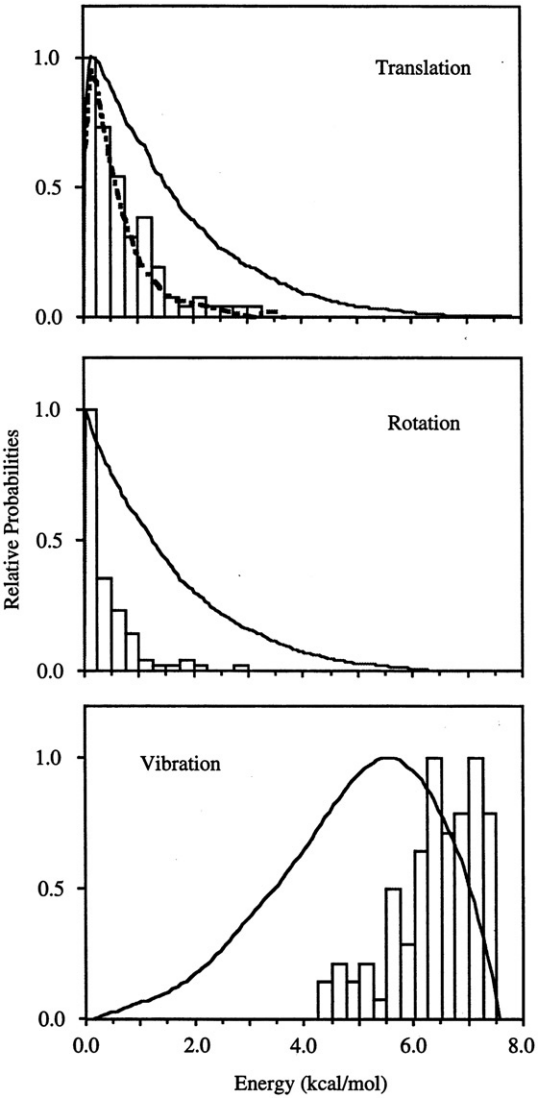

Figure 4. Product energy distribution for the $Cl^- \cdots CH_3Br \rightarrow ClCH_3 + Br^-$ reaction: histogram, trajectory result [28]; dashed line, experiment [103]; and solid line, prediction of OTS/PST [41].

translational energy. There is excellent agreement between the simulation and experimental studies.

3.2. $C_2H_5F^{\ddagger} \rightarrow C_2H_4 + HF$

3.2.1. *Comparison with experiment*

In a systematic set of experiments by Setser and coworkers [106–108], vibrational energy distributions of the HX product from the decomposition of chemically activated

haloalkanes were obtained by infrared chemiluminescence. One of the most carefully studied molecule is C_2H_5F formed by $H + C_2H_4F$ recombination, which activates $C_2H_5F^*$ with $E^{\ddagger} = 42.9$ kcal/mol, the energy in excess of its $C_2H_5F^* \rightarrow C_2H_4 + HF$ dissociation barrier. The HF vibration energy distribution has also been measured for C_2H_5F dissociated by infrared multiple photon absorption [109]. These experiments are thought to lead to $C_2H_5F^*$ molecules which dissociate with $E^{\ddagger} \cong 20$–35 kcal/mol.

To model the product energy partitioning for $C_2H_5F^*$ dissociation, direct dynamics simulations were performed [29,30] with trajectories initialized at the dissociation TS in accord with the microcanonical ensemble assumed by RRKM theory. These simulations were performed at the MP2 level of theory using both the 6–31G* and 6–311++G** basis sets. Their values for the exit-channel potential energy barrier release E_r^o are 45.3 and 50.6 kcal/mol, respectively. The latter value, for the larger basis set, is in excellent agreement with the experimental value of 49 ± 2 kcal/mol [108].

To directly compare with the experiments of Setser and coworkers a simulation was performed with a TS vibration and reaction coordinate translation energy $E_{vt}^{\ddagger}$ of 42 kcal/mol above the zero-point level. To further analyse the product energy partitioning, additional simulations were performed for $E_{vt}^{\ddagger}$ of 32 and 3.45 kcal/mol. The HF vibrational energy distribution calculated for $E_{vt}^{\ddagger}$ of 32 kcal/mol may be compared with that measured by Quick and Wittig [109] in infrared multiphoton dissociation of C_2H_5F. For each of the simulation studies, $RT/2$ (300 K) of rotational energy was added to each of the TS's rotation axes. Each trajectory contains ZPE in the vibrational modes orthogonal to the reaction coordinate. The results of the simulations are given in Table 1 and Figure 5. The average percentage of the available energy partitioned to $HF + C_2H_4$ relative translation, C_2H_4 vibration and rotation, and HF vibration and rotation are listed in Table 1. For the $E_{vt}^{\ddagger} = 42$ kcal/mol simulation the percentage of available energy partitioned to HF vibration is 14% for the larger basis set and in excellent agreement with the 15% value found from experiment. The smaller basis set underestimates the partitioning to HF vibration.

The populations of the HF vibration states $P(n)$, found from the simulations, are compared with experiment in Figure 5. Overall, the simulations with the 6–311++G**

Table 1. Average $C_2H_5F \rightarrow C_2H_4 + HF$ product energy partitioning for MP2/6–31G* and MP2/6–311++G** direct dynamics.[a]

		MP2/6–31G*			MP2/6–311++G**		
Product energy	$E_t^{\ddagger}=$	3.45	27	42	3.45	32	42
Rel trans		75.4	56.8	49.7	67.8(1.2)[b]	48.2(1.0)	46.2(1.0)
C_2H_4 vib		6.1	24.2	31.5	6.8(0.7)	26.2(0.8)	29.3(0.6)
C_2H_4 rot		4.6	5.9	6.0	5.1(0.3)	5.5(0.3)	6.2(0.3)
HF vib		10.5	8.7	7.9	16.9(1.3)	15.8(1.1)	14.0(1.0)
HF rot		3.4	4.4	4.9	3.4(0.4)	4.3(0.4)	4.3(0.3)

Notes: [a]The average energy partitioning is given in percent. In addition to the TS's vibration/reaction coordinate translation energy $E_t^{\ddagger}$, the TS also contains $3RT/2$ rotation energy ($T = 300$ K). Energies are given in kcal/mol. Zero-point energy is not included in the C_2H_4 and HF vibration energies.
[b]The uncertainty, in parentheses, is the standard deviation of the mean.

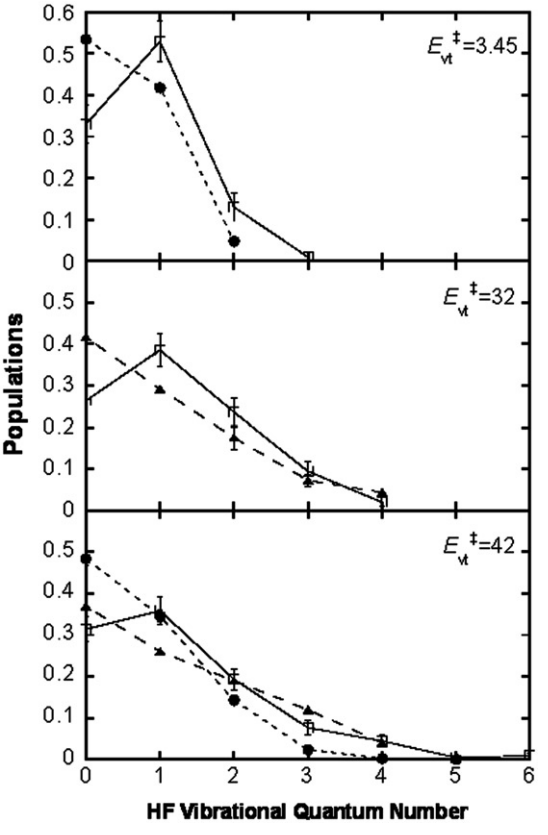

Figure 5. Populations of the HF vibrational states for $C_2H_5F \rightarrow HF + C_2H_4$ dissociation, with different amounts of vibration/reaction coordinate $E_{vt}^{\ddagger}$ in the $C_2H_5F^{\ddagger}$ transition state. □, results of the MP2/6–311++G** simulations; ●, results of the MP2/6–31G* calculations; and ▲, experimental results. The experimental results for $E_{vt}^{\ddagger}$ of 32 and 42 kcal/mol are from [109] and [108], respectively. (Reprinted with permission from J. Phys. Chem. A. **110**, 1484. Copyright 2006. American Chemical Society.)

basis set gives $P(n)$ in good agreement with the experiments at $E_{vt}^{\ddagger}$ of 32 and 42 kcal/mol. The major difference between the simulations and experiments is that the simulations give an inverted $P(1)/P(0)$ ratio, while the experiments do not. The 6–31G* calculations do not adequately populate the higher HF vibrational states and underestimate the partitioning to HF vibration.

3.2.2. *Partitioning of the exit-channel potential energy barrier release*

The total internal energy $E^{\ddagger}$ of the TS for each simulation is the TS's vibration and reaction coordinate translation energy $E_{vt}^{\ddagger}$ plus its average rotational energy of $3RT/2 = 0.89$ kcal/mol. The total energy available to the products is $E^{\ddagger}$ plus the potential energy release E_r^o in moving from the TS to the products, which is 45.33 and 50.62 kcal/mol for the 6–31G* and 6–311++G** calculations, respectively. Zamir and Levine [110]

Table 2. Parameters describing the partitioning of the excess energy and the potential energy release for $C_2H_5F \rightarrow HF + C_2H_4$.[a]

	MP2/6–31G*		MP2/6–311++G**	
	a_i	E_i^o/E_r^o	a_i	E_i^o/E_r^o
Rel trans	0.170	0.81	0.140	0.73
C_2H_4 vib	0.640	0.00	0.620	0.02
C_2H_4 rot	0.076	0.05	0.074	0.05
HF vib	0.046	0.11	0.110	0.18
HF rot	0.067	0.03	0.550	0.03

Note: [a]a_i represents the fraction of the excess energy at the TS partitioned to a particular type of energy. E_i^o/E_r^o is the fraction of exit-channel potential energy barrier release partitioned to a particular type of energy.

suggested that the average value for each type of product energy (E_i) and the TS total energy have the linear relationship

$$\langle E_i \rangle = E_i^o + a_i E^{\ddagger} \tag{14}$$

where the a_i give the fractions of $E^{\ddagger}$ partitioned to the different product energies and the E_i^o gives the parts of E_r^o which go to the different product energies. Summing Equation (14) over i gives

$$\sum \langle E_i \rangle = \sum E_i^o + E^{\ddagger} \sum a_i \tag{15}$$

where the sum of the a_i equals unity. The ratio E_i^o/E_r^o is the fraction of the exit-channel potential energy release, E_r^o, partitioned to product energy i.

As shown in Table 2, overall, the fitted parameters for the two basis sets are in very good agreement, with the only substantial differences for relative translation and HF vibration. The 6–31G* a_i values for relative translation and HF vibration are 0.03 and 0.06 larger and smaller than their 6–311++G** counterparts, respectively. The differences in the E_i^o/E_r^o are somewhat larger, with the 6–31G* values for relative translation and HF vibration 0.08 and 0.07 larger and smaller, respectively.

It has been suggested that the TS's statistical distribution of energy is maintained as the reactive system moves from the TS to products [111]. The a_i values in Equation (14) are fixed by the distribution of the excess energy at the TS, and this distribution is assumed to be unaffected by the dynamics as the ensemble of trajectories moves from the TS to products. Thus, the model predicts the same set of a_i values for the 6–31G* and 6–311++G** simulations, since both sample the same energy distribution at the TS. The a_i values in Table 2 are consistent with this model except for HF vibration, whose 6–311++G** a_i is a factor of 2 larger. Given the statistical uncertainties in the product energy partitionings (see Table 1), there are no significant differences in the a_i for relative translation or for the other product energies. The different a_i values for HF vibration indicate that the statistical distribution at the TS may be perturbed by the exit-channel dynamics.

Table 3. Comparison of QCT and ST calculations for model $CHCl_2CCl_3 \rightarrow C_2Cl_4 + HCl$ dissociation.[a]

Product energy	QCT[b]	ST
Rel trans	43.2 ± 0.5	39.7
C_2Cl_4 vib	43.1 ± 0.8	38.1
C_2Cl_4 rot	0.3 ± 0.0	0.2
HCl vib	9.8 ± 0.9	16.1
HCl rot	3.7 ± 0.4	5.9

Notes: [a]The calculations were performed at the MP2/6–31G* level of theory for the $C_2H_5F \rightarrow HF + C_2H_4$ potential energy surface. The reaction coordinate translational energy $E_t^{\ddagger}$ is 1.0 kcal/mol.
[b]The uncertainty is the standard deviation of the mean.

In an attempt to summarize experimental data for a series of HX elimination reactions, it has been suggested that, for $C_2H_5F \rightarrow HF + C_2H_4$ dissociation, the partitioning of the exit-channel potential energy is 20%, 45%, 24%, and <12% to relative translation, C_2H_4 vibration and rotation, HF vibration, and HF rotation [108]. As shown in Table 1, the results of the simulations are strikingly different from this predicted energy partitioning. For both the 6–31G* and 6–311++G** simulations, the partitioning of the potential energy to C_2H_4 vibration energy is negligible, in contrast to the large partitioning inferred from summarizing the experimental data. A possible origin of this difference between the partitioning of E_r^o, found from the simulations and inferred from the experiments, is the assumption made, in summarizing the experiments, that partitionings of the exit-channel potential barrier for different HX eliminations are similar, regardless of the masses of the substituent atoms. For example, the energy released to relative translation for $C_2H_5F \rightarrow HF + C_2H_4$ dissociation was deduced from experiments for $CH_3CCl_3 \rightarrow HCl + C_2H_2Cl_2$ dissociation [112].

A possible mass effect for the product energy partitioning was investigated by retaining the $C_2H_5F \rightarrow HF + C_2H_4$ MP2/6–31G* PES, but changing the masses of the substituent atoms in the direct dynamics simulation to model $CHCl_2CCl_3 \rightarrow C_2Cl_4 + HCl$ dissociation. A small $E^{\ddagger} = 1.0$ kcal/mol was used so that it would only make a small contribution to the energy available to the reaction products. In this way, the product energy partitioning reflects the exit-channel potential energy release. The calculated average percentage energy transfers are listed in Table 3. The simulation for the $CHCl_2CCl_3$ model partitions nearly equal amounts to relative translation and C_2H_4 vibration, i.e. 43.2% and 43.1%. In contrast, the simulation for C_2H_5F partitions 75.4% of the available energy to relative translation and only 6.1% to C_2H_4 vibration (see Table 1). Thus, an important mass effect is seen in these simulations of HX elimination. The differences in the other energy partitionings for C_2H_5F and $CHCl_2CCl_3$ dissociation are much smaller. Mass effects for partitioning of exit-channel potential energy barrier release E_r^o are considered in more detail below, using a single trajectory (ST) model.

3.2.3. *A single trajectory model for partitioning of* E_r^o

A single trajectory (ST) model was tested for determining how the exit-channel potential energy release E_r^o is partitioned to product energies and was found to give accurate

Table 4. Comparison of QCT and ST calculations for $C_2H_5F \rightarrow C_2H_4 + HF$ product energy partitioning.[a]

	MP2/6–31G*		MP2/6–311++G**	
Product energy	QCT	ST	QCT[b]	ST
Rel trans	75.4	70.7 (74.9)	67.8 ± 1.2	60.1 (64.1)
C_2H_4 vib	6.1	6.5 (6.8)	6.8 ± 0.7	5.4 (5.5)
C_2H_4 rot	4.6	1.4 (1.5)	5.1 ± 0.3	2.4 (2.4)
HF vib	10.5	19.1 (14.4)	16.9 ± 1.3	28.6 (24.1)
HF rot	3.4	2.3 (2.4)	3.4 ± 0.3	3.5 (3.9)

Notes: [a]The values listed are the percentage energy transfers. The reaction coordinate translational energy $E_t^{\ddagger}$ equals 3.45 kcal/mol for the calculations. QCT is quasiclassical trajectory and ST is a single trajectory; see text. The ST results inparentheses are for $E_t^{\ddagger} = 1.0$ kcal/mol.
[b]The uncertainty is the standard deviation of the mean. This uncertainty was not calculated for the MP3/6–31G* calculation, but it is expected to be approximately two times smaller since the sample size is four times larger.

results for HX elimination from haloakanes, when compared with the above quasiclassical trajectory (QCT) method [31]. For the ST model no ZPE is added to the TS's vibrational modes, no rotational energy is added, and a small value of energy is added to reaction coordinate translational $E_t^{\ddagger}$. This results in a unique trajectory since it is only defined by $E_t^{\ddagger}$ and its momentum directed towards products. The QCT method has the same value of $E_t^{\ddagger}$ and no rotational energy, but there is ZPE in the TS's vibrational modes. With the phase averaging for the QCT simulation, an ensemble of trajectories is calculated instead of a single trajectory. The absence of phase averaging in the ST model is akin to the approach used by Giese and Gentry in developing the DECENT model [113].

Listed in Table 4 are the average percentages of the total available energy partitioned to the different product degrees of freedom, for the $C_2H_5F \rightarrow C_2H_4 + HF$ QCT and ST calculations. The calculations are performed using both the MP2/6–31G* and MP2/6–311++G** PESs. A comparison of the QCT and ST results, for $E_t^{\ddagger} = 3.45$ kcal/mol, shows that they give the same pattern for the product energy partitioning. This is found for both basis sets. Most of the energy is partitioned to relative translation, with HF vibration the next major important recipient of the available energy. The ST calculations distribute approximately a factor two more of the available energy to HF vibration as compared to QCT, with the additional energy primarily coming from relative translation and C_2H_4 rotation. The difference in the HF vibrational energy, for the QCT and ST calculations, may arise from the treatment of the HF ZPE. This degree of freedom is formed in moving from the TS to products and initially does not have ZPE. Subtracting ZPE from HF vibration for the QCT calculation, but not for the ST calculation, may affect their product energy partitionings. In the future it may be useful to test a ST model in which ZPE is subtracted from product modes, which are not present at the TS and formed in moving from the TS to products. Nevertheless, the current ST calculations establish the nature of the product energy partitioning. The ST calculation at $E_t^{\ddagger} = 1.0$ kcal/mol gives a similar product energy partitioning (values in parentheses) to the ST result at $E_t^{\ddagger} = 3.45$ kcal/mol.

Both QCT and ST calculations with $E_t^{\ddagger} = 1.0$ kcal/mol were performed, for the above $CHCl_2CCl_3$ model, to again test the ST approach. The average percentage energy transfers are listed in Table 3 and the product energy distributions for the QCT calculations are plotted in Figure 6. The arrows in these plots denote the energy partitioning given by the ST. The product energy partitioning from the ST is very similar to the average energy partitioning for the QCT ensemble, providing additional evidence for the utility of the ST approach for establishing the pattern of product energy partitioning in unimolecular dissociation. The utility of the ST approach agrees with previous trajectory studies by Schinke [114] of photodissociation. When photodissociation is fast and direct, a single trajectory, started at the Franck Condon point on the upper potential energy surface, gives a good approximation to the maxima of the product energy distributions. It is also noteworthy that Kaledin and Miller have found that a single trajectory may give meaningful results in initial value representation (IVR) semiclassical calculations [115].

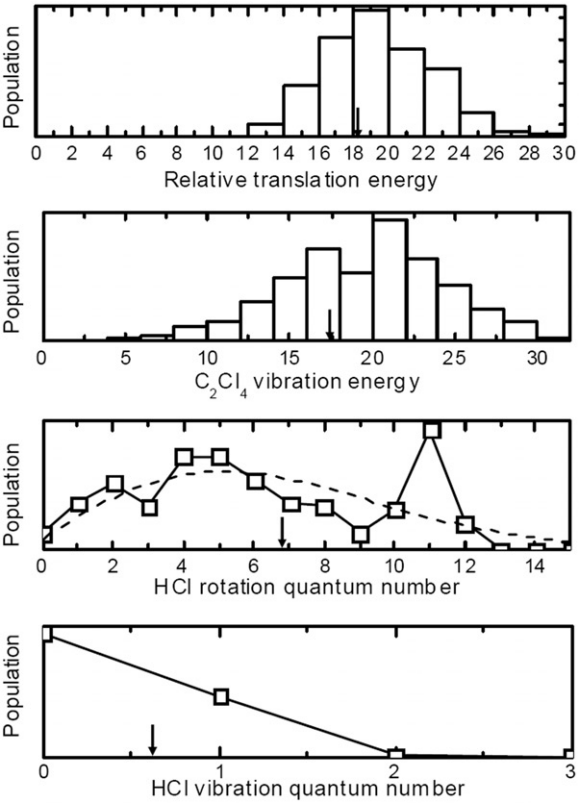

Figure 6. Distributions of relative translation, C_2Cl_4 vibration energy and HCl vibration and rotation quantum numbers for the QCT calculation of model $CHCl_2CCl_3$ dissociation, with $E_t^{\ddagger} = 1.0$ kcal/mol and zpe in the TS's vibration modes. The C_2H_5F MP2/6–31G* PES was used for the direct dynamics simulation. The C_2Cl_4 rotation energy is quite small and its distribution is not shown. The arrows denote the ST product energy partitioning. (Reprinted with permission from J. Chem. Phys. **124**, 064313. Copyright 2006. American Institute of Physics.)

It is important to recognize that the ST approach is not a panacea for chemical dynamics, since at best it can only represent the average (or possibly most probable) values of product energy distributions. If a distribution is bi- or multimodal, using an ST will certainly be problematic. The use of a ST will also be inappropriate if there are multiple product channels in proceeding from the TS [5,47]. The ST approach will be inapplicable if a potential energy well exists in the exit-channel that traps the reactive system and leads to chaotic dynamics before forming products. For such a system, a slight change in the initial condition at the TS would give a completely different trajectory. Kaledin and Miller have previously discussed the inapplicability of the ST approach in semiclassical calculations [115], if the trajectory is chaotic.

3.2.4. *Mass effects for product energy partitioning*

To investigate in more detail possible mass effects for the product energy partitioning, ST calculations were performed for HX elimination from a halogenated ethane by using the C_2H_5F MP2/6–31G* PES and varying the masses of the atoms. The masses of H and F were changed to those of chlorine and, as an extreme test case, to a mass of 500 amu (denoted by M). For this test case the carbon atoms were also changed to the mass M. The energy partitioning determined from these ST calculations are listed in Table 5, with results given for $E_t^{\ddagger}$ of both 1.0 and 3.45 kcal/mol. In discussing these simulations, the C-atom to which the halogen is bonded is identified as C1, while the other carbon is C2 (see Figure 7).

Table 5. Product energy partitioning for single trajectories using the $C_2H_5F \rightarrow C_2H_4 + HF$ potential energy surface.[a]

Molecule[b]	$E_t^{\ddagger}$	Rel. trans.	Vib[c]	Rot[c]	HX vib	HX rot
C_2H_5F	1.0	74.9	6.8	1.5	14.4	2.4
	3.45	70.7	6.5	1.4	19.1	2.3
C_2H_5Cl	1.0	75.6	5.9	2.4	15.9	0.1
	3.45	72.2	6.0	2.3	19.4	0.1
C_2H5M	1.0	70.3	4.8	4.9	16.5	3.5
CH_3MH_2F	1.0	72.1	5.2	4.7	14.8	3.2
MH_3MH_2M	1.0	73.9	4.4	4.3	15.6	1.8
MH_3CH_2F	1.0	55.0	8.0	20.3	14.9	1.8
$CHCl_2CH_2Cl$	1.0	43.9	14.2	26.0	15.8	0.1
CH_3CCl_3	1.0	47.3	24.4	11.5	15.7	1.1
	3.45	44.9	23.6	11.0	19.5	1.0
$CHCl_2CCl_3$	1.0	39.7	38.1	0.2	16.1	5.9
	3.45	37.6	36.8	0.1	19.5	6.0

Notes: [a]The calculations were performed at the MP2/6–31G* level of theory. The values listed are the percent energy transfers.
[b]M is an artificial very heavy atom with a mass of 500 amu. The last atom in the molecular formula is the halogen that dissociates. The HX dissociations are four centred, with the H and *X* atoms dissociating from different C atoms.
[c]Vib and rot are the vibration and rotation energies of the ethylene product.

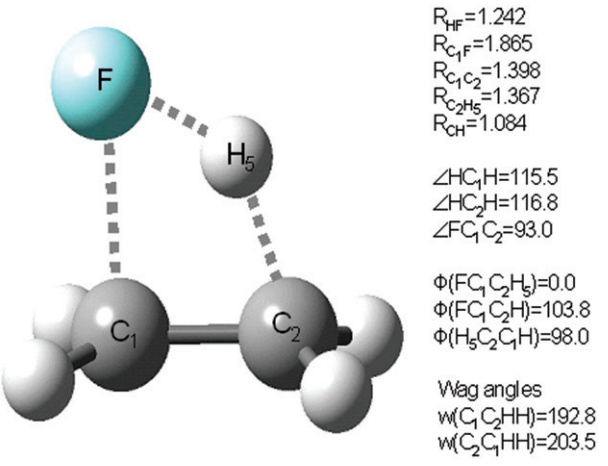

Figure 7. [Colour online] Transition state structure for $C_2H_5F \rightarrow HF + C_2H_4$ dissociation. Calculation at the MP2/6–31G* level of theory. The units for bond lengths and angles are angstroms and degrees. (Reprinted with permission from J. Chem. Phys. **124**, 064313. Copyright 2006. American Institute of Physics.)

A number of important features for the product energy partitioning are identified in Table 5. An immediate observation is that there is very little variation in the per-cent energy transfer to HX vibration. Previous trajectory studies for $C_2H_5F \rightarrow C_2H_4 + HF$ dissociation [29] have shown that HF elimination may be viewed as a process in which the HF bond is first formed and then HF directly leaves C_2H_4, due to the repulsion of the exit-channel potential. Excitation of the HF stretch occurs in a very short time and, therefore, the HF vibration is decoupled from the C_2H_4 vibrations. For this model, the product energy partitioning should not be significantly affected by only changing the mass of the F- or C-atoms, and this is indeed the result observed in the simulations for C_2H_5Cl, C_2H_5M, CH_3MH_2F, and MH_3MH_2M.

Changing the mass of the C-atoms affects the energy partitioning to relative translation and olefin vibration and rotation. For MH_3CH_2F, the partitioning to MH_2CH_2 rotation is increased to 20% and relative translation is lowered to 55%. In contrast, the energy partitioning for CH_3MH_2F is nearly identical to that for C_2H_5F. The difference in the energy partitioning for MH_3CH_2F and CH_3MH_2F is easily understood by considering the TS structure in Figure 7. The HF product recoils from the C1 atom. For CH_3MH_2F, HF recoils off the massive M atom, near the centre of mass of CH_2MH_2. As a result, a small angular momentum and rotational energy (i.e. 4.7 percent) is transferred to the CH_2MH_2 product. However, for MH_3CH_2F, the centre of mass of MH_2CH_2 is located at the M-atom, not the C1 atom, and a substantial amount of rotation energy is transferred to MH_2CH_2; i.e. 20.3 percent. This energy comes from relative translation, with no significant changes in the HF energies or the ethylene vibration energy.

The position of the centre of mass of the dissociating molecule also affects the partitioning of energy to olefin rotation for $CHCl_2CH_2Cl$, CH_3CCl_3, and $CHCl_2CCl_3$. Of all the molecules studied, the largest percentage partitioning to olefin rotation is for $CHCl_2CH_2Cl$ dissociation. This is consistent with this dissociation having the largest

separation between the C1 carbon atom from which the chlorine atom dissociates and the product's centre of mass, which is located near the chlorine atoms of the product's CCl_2 group. This separation is slightly smaller for MH_3CH_2F dissociation and as a result, its olefin product receives a somewhat smaller partitioning to rotation than does $CHCl_2CH_2Cl$ dissociation; i.e. 20.3 versus 26.0%. For CH_3CCl_3 dissociation, the olefin product's centre-of-mass is also located near the chlorine atoms of the CCl_2 group, but the distance from the centre-of-mass to the C1 atom is much smaller than for $CHCl_2CH_2Cl$ and, as a result, the percentage transfer to olefin rotation is smaller. For $CHCl_2CCl_3$ dissociation, the CCl_2CCl_2 product molecule is symmetric with heavy atoms at both of its ends and a very large moment of inertia. It receives very little rotational energy.

For the simulations at $E_t^{\ddagger} = 1.0$ kcal/mol, the ordering of the molecules by their energy partitioning to olefin vibration is $MH_3MH_2M < C_2H_5M < CH_3MH_2M < C_2H_5Cl < C_2H_5F < CHCl_2CH_2Cl < CH_3CCl_3 < CHCl_2CCl_3$, with respective percents of $4.4 \sim 4.8 \sim 5.1 \sim 5.9 \sim 6.8 \sim 8.0 < 14.2 < 20.4 < 38.1$. Energy release to the vibration of the olefin product is clearly more efficient for the latter three dissociations, with only a 3.6% variation in the release to olefin vibration for the first six molecules. Insight into the origin of the enhanced partitioning to olefin vibration, for the last three molecules, was obtained by plotting the internal coordinates of the olefin product versus time. This analysis for $CHCl_2CCl_3 \rightarrow HCl + CCl_2CCl_2$ dissociation shows that 2/3–3/4 of the product CCl_2CCl_2 vibration energy resides in the out-of-plane CCl_2 wag–bend motions.

Two factors give rise to the substantially different wag–bend excitations for $CHCl_2CH_2Cl$, CH_3CCl_3, and $CHCl_2CCl_3$ dissociation as compared to C_2H_5F dissociation, and they both are related to the difference in the masses of the chlorine and H atoms of the product olefin. The bonds of both HCl and HF are formed within 8 fs after the system leaves the TS [29]. Within this short time, there is very little change in the CCl_2 wag angles from their TS values as a result of their long vibration period of 75 fs. Thus, a Franck–Condon type model [116–118] seems appropriate for describing the CCl_2 wag–bend motions with respect to the rapid HCl bond formation. In contrast, the CH_2 wag bends for C_2H_5F dissociation undergo some relaxation to their 180° equilibrium values within the 8 fs for HF bond formation, as a result of their shorter period of 35 fs. This appears to be the principal mechanism for exciting the CCl_2 wag–bend for $CHCl_2CH_2Cl$ dissociation.

The above Frank–Condon model is responsible for only a small portion of the wag–bend excitation for CH_3CCl_3 and $CHCl_2CCl_3$ dissociation. The remainder of this excitation is also a mass effect. As HCl pushes off the C1 carbon atom, the chlorine atoms bonded to it move very little, because of their substantial mass, and the CCl_2 wag–bend receives kinetic energy from the C1-atom's motion. For C_2H_5F dissociation the much lighter H-atoms move with the C1-atom and the wag motion does not receive this substantial amount of kinetic energy.

4. Non-statistical dynamics

4.1. *Cyclopropane stereomutation*

Renewed interest in the decomposition of cyclopropanes and the role of the trimethylene biradical in the decomposition has been fuelled by two experiments that give apparently irreconcilable results [119,120]. Experiments of *S*,*S*-trans-cyclopropane-1,2-d_2 at 695 K

indicate that the rate of isomerization via double-terminal rotation k_{12} (i.e. con- and disrotation of the terminal methylene groups) is at least five times faster than that for isomerization via single-terminal rotation k_1 [119]. Similar experiments with chiral cyclopropanes-[1-^{13}C]1,2,3,-d_3 at 680 K yield a k_{12}/k_1 ratio of 1.0 ± 0.2 [120].

To obtain the k_{12}/k_1 ratio from experimental data (e.g. the *trans* → *cis* rate for cyclopropane structural isomerization) requires the use of a kinetic scheme that includes the role of the trimethylene biradical, and identifying the appropriate model for its dynamics is of pivotal importance [34,121–123]. Trimethylene has a very shallow potential energy minimum, which lies ~60 kcal/mol above the cyclopropane minimum (see Figure 8) [124]. It mediates both the geometric and structural isomerizations of cyclopropane, which result in cyclization and propene formation, respectively. The pathways for geometric isomerization have low barriers (Table 6). Structural isomerization has barrier of ~7 kcal/mol with respect to the trimethylene potential energy minimum. Cyclopropane may decompose to form trimethylene via three different ring opening pathways: conrotation (CON) and disrotation (DIS) paths in which both terminal methylenes rotate, and a *cis–trans* (CT) path with a single methylene rotation. Cyclization of trimethylene, and formation of the geometric isomers, also occurs via these three pathways.

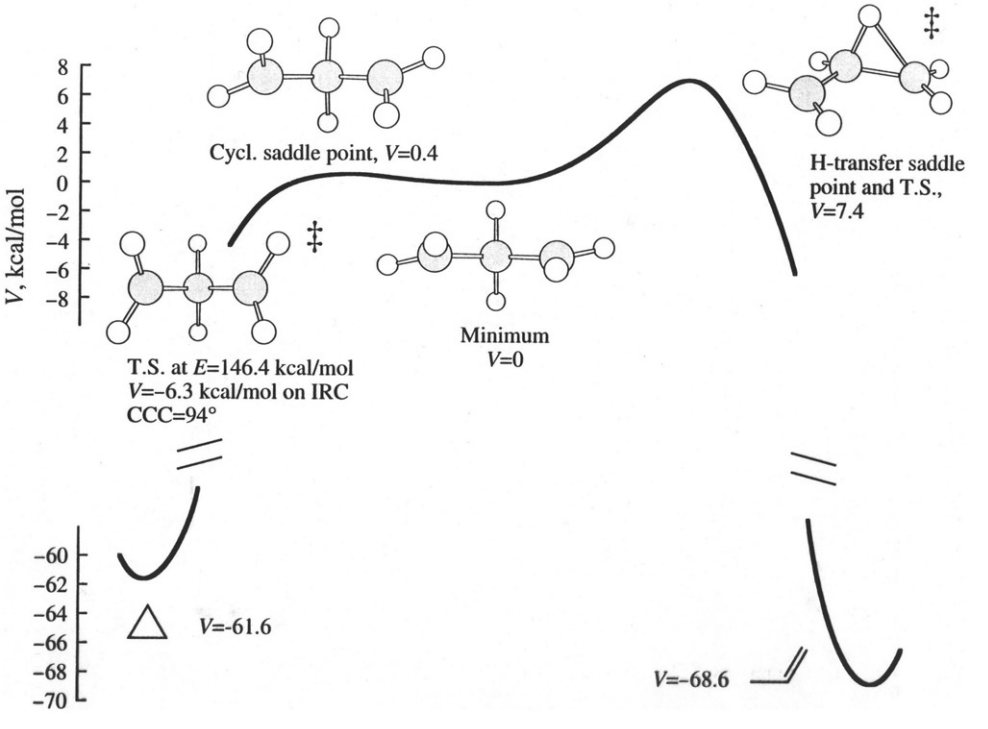

Figure 8. Minimum potential energy along the cyclopropane ↔ propene reaction path; the curve linking the stationary points merely serves to illustrate connectivity. (Reprinted with permission from J. Am. Chem. Soc. **118**, 9922. Copyright 1996. American Chemical Society.)

Semiempirical direct dynamics were used to study trimethylene's unimolecular dynamics and thermal stereomutation of cyclopropane [32,34,35]. The semiempirical model used in these simulations is AM1 with specific reaction parameters (SRPs) [125] chosen to fit the CASSCF PES [124]. To simulate the high-pressure thermal unimolecular decomposition of cyclopropane and its stereomutation, it was assumed that RRKM theory is valid for cyclopropane's unimolecular dynamics, so that Boltzmann distributions of reacting molecules could be sampled at the CON‡, DIS‡, and CT‡ transition states for the cyclopropane $\rightarrow$ trimethylene unimolecular reaction [35]. Each trajectory was integrated forward and backward in time until either propene or an isomer of cyclopropane was formed. In this way, the isomerization dynamics was obtained for the ensemble of trajectories. To compare with experiment [119,120] the trajectories were further analysed to determine whether cyclization followed single rotation versus double rotation of trimethylene's terminal methylenes, that is a ratio k_1/k_{12} of single/double rotation rate constants.

The trajectory simulations show that the unimolecular dynamics of trimethylene formed by the trajectories initiated at the CON‡, DIS‡, and CT‡ TSs are not statistical [34,35]. The statistical model assumes energy rapidly becomes randomized in the trimethylene intermediate so that the probability a trajectory cyclizes via the CON, DIS, or CT path depends on only the trimethylene energy and not on which TS is excited, i.e. CON‡, DIS‡, and CT‡. As shown in Table 6, the trajectory dynamics do not support such a model. The CON path has the lowest barrier for cyclization of 0.4 kcal/mol, while the 2.6 kcal/mol barrier for the DIS path is the highest. For the trajectories initiated at the CT‡ TS, the majority follow the CT path, with less than 10% if the cyclization occurring via the CON path. For the trajectories initiated at the DIS‡ TS, the majority follow the CT path. Only for the ensemble of trajectories excited at the CON‡ TS does the branching between the CON, DIS, and CT paths follow the statistical type dynamics expected from E_o barriers. The trimethylene unimolecular dynamics is strongly non-RRKM.

The dynamics of the classical trajectories support a mechanistic continuum for trimethylene decomposition encompassing concerted and non-concerted processes in which non-statistical effects are paramount [34], with the dynamics possibly becoming statistical for the few long-time events [126]. Most double rotation trajectories undergo a

Table 6. Cyclization mechanisms following thermal excitation at the CON‡, DIS‡ and CT‡ transition states for cyclopropane $\rightarrow$ trimethylene decomposition.[a]

	Cyclization reaction path		
TS Excited[b]	CON $E_o = 0.4$[c]	DIS $E_o = 2.6$	CT $E_o = 1.8$
CON‡	65	9	26
DIS‡	29	16	55
CT‡	8	24	68

Notes: [a]The numbers are the percentages that follow the specific reaction paths.
[b]Trajectories are samples at the TS from a 695 K Boltzmann distribution.
[c]The barrier for cyclization, in kcal/mol, with respect to the trimethylene potential energy minimum.

single set of 180° rotations and cyclize immediately with an average lifetime of 130 fs. It seems appropriate to call them 'concerted'. On the other hand, the 430 fs average lifetime for the products formed by an overall single methylene rotation, accommodates multiple rotations and is more typical of an intermediate. Finally, the k_{12}/k_1 ratio of 2.9–3.5 determined from the trajectories lies between the experimental values of 1.0 ± 0.2 [120] and 5–50 [119], and is similar to the value of 4.7 reported by Hrovat *et al.* [127] from a trajectory simulation on an analytic PES. Their trajectory study also exhibits substantial non-statistical dynamics for trimethylene.

From the discussion given above, in Section 2.3, it is expected that classical chemical dynamics simulations will give the correct short-time intramolecular and unimolecular dynamics for trimethylene, if an accurate PES is used. There are uncertainties in the AM1-SRP PES used for the study reported here and the same may be the case for the PES used by Hrovat *et al.* [127]. The current studies correctly identify the non-statistical, non-RRKM dynamics for trimethylene, but the PESs may not yield quantitative properties such as the k_{12}/k_1 rate constant ratio. The current studies also identify the difficulty in modeling cyclopropane steromutation since the trimethylene kinetics is neither statistical or direct. For the former RRKM theory would be applicable and for the latter one could assume the trajectories pass directly through the trimethylene potential energy minimum and remain on the CON, DIS, and CT reaction paths. It will be of interest to re-investigate the trimethylene dynamics with more accurate PESs.

4.2. *Central barrier dynamics for the $Cl^- + CH_3Cl$ S_N2 nucleophilic substitution reaction*

As described above, in Section 3.1, the dynamics of gas-phase S_N2 nucleophilic substitution reactions of the type given by reaction (12) are highly non-statistical. These dynamics are present in the $Cl^- + CH_3Cl$ S_N2 reaction [36–46], whose reaction path potential energy curve is depicted in Figure 3. The statistical model for the reaction assumes the $Cl^- + CH_3Cl$ reactants associate, with a rate constant given by the ion–molecule capture model, to form a $Cl^- \cdots CH_3Cl$ ion–dipole complex with randomization of its internal energy. RRKM theory may then be used to calculate the unimolecular rate constants for dissociation of $Cl^- \cdots CH_3Cl$ to the $Cl^- + CH_3Cl$ reactants and isomerization to $CH_3Cl \cdots Cl^-$ by crossing the central barrier. With randomization of vibrational energy in the $CH_3Cl \cdots Cl^-$ post reaction complex, its isomerization and dissociation rate constants are also given by RRKM theory and the $CH_3Cl + Cl^-$ product energy partitioning given by OTS/PST theory. Since the isomerization rate constant is much smaller than the dissociation rate constant for the ion–molecule complexes, crossing the central barrier is rate controlling and the statistical model assumes the S_N2 rate constant is given by TST. However, the actual reaction dynamics for the $Cl^- + CH_3Cl$ S_N2 reaction are non-RRKM and non-TST as illustrated below by trajectories initiated at the $[Cl \cdots CH_3 \cdots Cl]^-$ central barrier, which were first studied with an analytic PES fit to HF/6–31G* *ab initio* calculations [39] and more recently investigated by MP2/6–31G* [45] direct dynamics.

TST assumes there is a Boltzmann distribution of states at the TS and one way to investigate the dynamics of the pre- and post-reaction $Cl^- \cdots CH_3Cl$ complexes is to form them by initiating the trajectories at the $[Cl \cdots CH_3 \cdots Cl]^-$ central barrier, in accord with this Boltzmann distribution, and integrate the trajectories in both the forward and

reverse direction. The average trajectory predicted by harmonic RRKM theory [39] for a 300 K Boltzmann distribution at the TS, identified by $g_a = r_{C-Cl_a} - r_{C-Cl_b} = 0$, is illustrated in Figure 9(a). The harmonic RRKM lifetime for the $Cl^- \cdots CH_3Cl$ complexes is 2 ps and the average complex has ~7 $Cl^- \cdots CH_3Cl$ stretching vibrational periods before it dissociates to $Cl^- + CH_3Cl$. Including anharmonicity in the RRKM calculation increases the complexes' lifetime to 4 ps [42], with ~14 stretching vibrational periods before dissociation.

For the central barrier dynamics investigated with the analytic PES [39], 200, 300, 1000, and 2000 K Boltzmann distributions, including ZPE, were sampled at the central barrier TS and the trajectories were integrated for up to 20 ps in each direction. RRKM theory predicts the fraction of $Cl^- \cdots CH_3Cl$ complexes that remain undissociated is $\exp(-t/\tau)$, where t is the integration time and τ the complexes' RRKM lifetime. For the 300 K simulation, with $t = 20$ ps and $\tau = 4$ ps, only 0.6% of the trajectories are predicted to remain undissociated. At 200 K this number is larger and ~3%. A striking finding from the simulations is the small probability that the complexes dissociate to the $Cl^- + CH_3Cl$ asymptotic limits. For the 200 K simulation, not one of the trajectories integrated in both the forward and reverse directions reached one of the asymptotic limits. Of the 150 trajectories calculated for the TS's 300 K Boltzmann distribution only one trajectory reached an asymptotic limit, and this limit was only attained for the integration in one direction. For the integration in the other direction the trajectory remained in a $Cl^- \cdots CH_3Cl$ complex. For the higher temperatures of 1000 and 2000 K, where essentially all the complexes are predicted to dissociate by RRKM theory, there is dissociation, but a significant fraction of the trajectories remain undissociated. The conclusion from these simulations is that the unimolecular dynamics is highly non-RRKM for the $Cl^- \cdots CH_3Cl$ complexes that participate in the S_N2 reaction.

Instead of dissociating, what the $Cl^- \cdots CH_3Cl$ complexes do is recross the central barrier, also highly non-RRKM dynamics. For $Cl^- \cdots CH_3Cl$ complexes containing an average energy concomitant with the average energy of the central barrier TS at 300 K, the RRKM rate constant to cross the central barrier is 1000 times smaller than to dissociate to $Cl^- + CH_3Cl$. A typical trajectory is illustrated in Figure 9(b). There are multiple crossings of the central barrier for both the forward and backward integrations, and at the end of these 20 ps integrations the trajectory is in the same complex. The recrossing of the TS means that TST will overestimate the S_N2 rate constant, but a quantitative value for the TST correction factor κ cannot be determined from the trajectories, since many did not reach the $Cl^- + CH_3Cl$ asymptotic limits during the trajectory integrations. As discussed above, this is particularly critical for the 200 and 300 K simulations. To approximate the number of reactions, any trajectory was counted as reactive if its backward and forward integrations ended on different sides of the central barrier. The resulting value of κ, given by the number of reactions divided by the number of central barrier recrossings, is ~0.1 for each of the temperatures investigated. This is clearly an underestimate of κ, since there would be more barrier recrossings if the trajectories were integrated longer so that both the forward and backward integrations terminated at the asymptotic limits.

The $[Cl \cdots CH_3 \cdots Cl]^-$ central barrier dynamics was also investigated using MP2/6–31G* direct dynamics [45]. Because of the computational expense of these trajectories, only a 300 K Boltzmann distribution was investigated at the central barrier and the trajectories were only integrated for 3 ps in both the forward and reverse

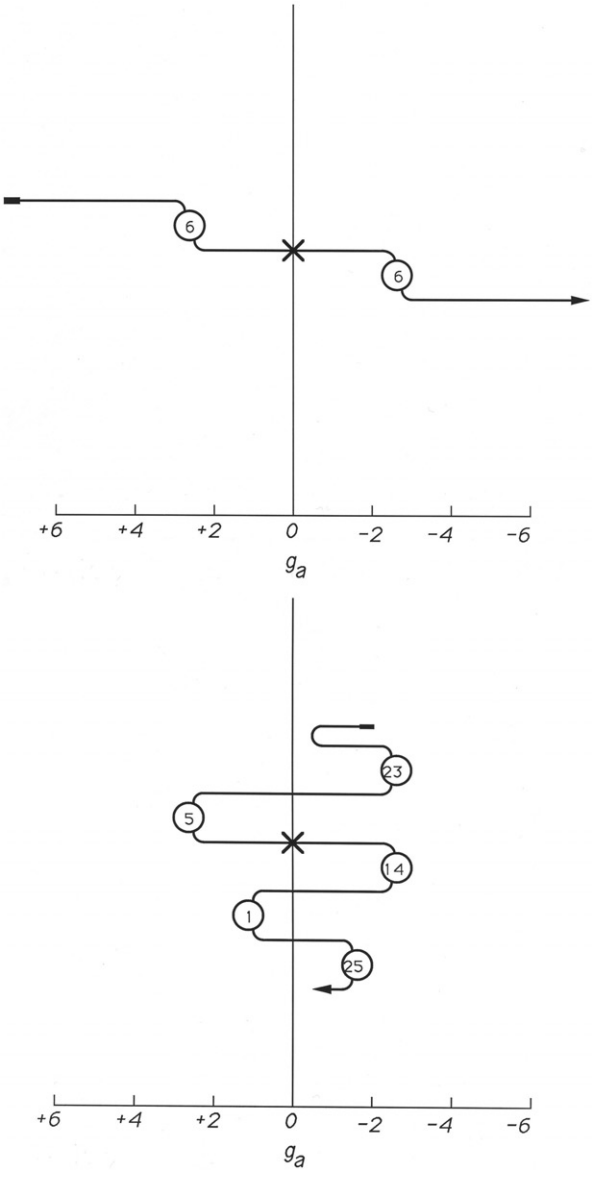

Figure 9. (a) The average trajectory predicted by harmonic quantum RRKM theory for a $T = 300$ K Boltzmann distribution at the $Cl^- + CH_3Cl \rightarrow ClCH_3 + Cl^-$ central barrier. g_a, given in angstroms, is the difference between the two C–Cl bond lengths. The numbers in the circles identify the number of inner turning poinys between Cl^- and the CH_3Cl moiety while the system is trapped in the ion–dipole complex. The *X* identifies the position where the trajectory is initialized; (b) same as (a) but for a representative trajectory for the $T = 1000$ K Boltzmann distribution. (Reprinted with permission from J. Chem. Phys. **96**, 8275. Copyright 1992. American Institute of Physics.)

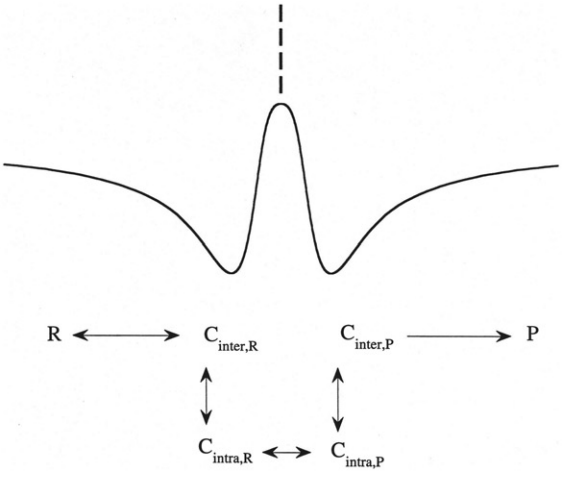

Figure 10. Dynamical model for S_N2 nucleophilic substitution. The labels R and P denote the reactant and product sides of the central barrier, respectively [41].

directions, as compared to the 20 ps integrations described above. The results of these direct dynamics trajectories are similar to those above for the analytic PES. Not one of the direct dynamics trajectories formed the $Cl^- + CH_3Cl$ products, in contradiction to the 50% dissociation, i.e. $\exp(-3/4)$, predicted by RRKM theory. Extensive recrossings of the central barrier were found and, using the analysis described above, a value of $\kappa = 0.2$ was determined. That it is larger than the above value of 0.1 is consistent with the integration of the direct dynamics trajectories for a shorter period of time.

A dynamical model for S_N2 nucleophilic substitution that emerges from these trajectory simulations and others for the $Cl^- + CH_3Cl$ system [36–46] is depicted in Figure 10 [41]. The complex formed by a collision between the reactants is an intermolecular complex $C_{inter,R}$. To cross the central barrier, this complex has to undergo a unimolecular transition in which energy is transferred from the intermolecular modes to the CH_3Cl intramolecular modes, which forms the intramolecular complex $C_{intra,R}$. The $C_{inter,R} \rightarrow C_{intra,R}$ rate does not involve the crossing of a potential energy barrier, but results from a dynamical barrier for energy transfer [39]. The intramolecular complex accesses the central barrier region of the potential energy surface and $Cl^- \cdots CH_3Cl \rightarrow ClCH_3 \cdots Cl^-$ isomerization occurs by a $C_{intra,R} \rightarrow C_{intra,P}$ transition. Products are formed when $C_{intra,P} \rightarrow C_{inter,P}$ occurs. Central barrier recrossings become important, as described above for the $Cl^- + CH_3Cl$ system, when the $C_{intra,R} \leftrightarrow C_{intra,P}$ transitions are faster than the transitions between the intermolecular and intramolecular complexes. This model also explains the $Cl^- \cdots CH_3Cl \rightarrow Cl^- + CH_3Cl$ dissociation kinetics for $Cl^- \cdots CH_3Cl$ complexes formed by $Cl^- + CH_3Cl$ association [42,45]. The initial unimolecular kinetics of this complex is represented by $C_{inter,R}$ with only there active degrees of freedom [42].

This dynamical model is also applicable to $Cl^- \cdots CH_3Br \rightarrow ClCH_3 + Br^-$ S_N2 nucleophilic substitution. As discussed above, in Section 3.1, simulations show that when the complex's low-frequency intermolecular modes are excited [28], it preferentially dissociates to $Cl^- \cdots CH_3Br$. However, this becomes a negligible reaction path, and

instead, $Cl^- \cdots CH_3Br \rightarrow ClCH_3 \cdots Br^-$ isomerization becomes important when the CH_3Br intramolecular modes are excited. Energy transfer between intermolecular and intramolecular modes is also inefficient for the $ClCH_3 \cdots Br^-$ complex, which does not immediately dissociate to $ClCH_3 + Br^-$ as predicted by RRKM theory but remains trapped for some time in the intramolecular complex formed by $Cl^- \cdots CH_3Br \rightarrow ClCH_3 \cdots Br^-$ isomerization. $Cl^- \cdots CH_3Br \rightarrow ClCH_3 \cdots Br^-$ central barrier recrossings are also important [28], contrary to the prediction of RRKM theory. The preferential dissociation, of the $C_{intra,R}$ complex to $C_{intra,P}$ for the $Cl^- + CH_3Br$ system, is also observed experimentally [96].

5. Non-IRC reaction paths and avoiding deep potential energy minima

A widely used paradigm in chemical kinetics and dynamics is the intrinsic reaction coordinate (IRC) [11], which assumes the reaction path is defined by paths of steepest descent connecting stationary points on the PES. This motion results from setting the velocity of each atom to zero after each infinitesimal step. The attraction of the IRC reaction path is that it provides well-defined structures between stationary points (i.e. transition states, potential energy minima, reactants and products) on the PES. A serious shortcoming of the IRC for gas-phase events is that, since energy is constant, there is not a single trajectory that actually has the motion defined by the IRC. Nevertheless the IRC concept is widely used, forming the basis of applications of variational transition state theory (VTST) [128], the reaction path Hamiltonian [129], and the vibrationally adiabatic theory of chemical kinetics [130,131].

The possible presence of non-IRC dynamics in chemical kinetics has been known for some time, and well-understood examples are triatomic $A + BC \rightarrow AB + C$ reactions with an early TS and substantial exit-channel potential energy release in moving from the TS to products [132]. The initial transfer of the exit-channel potential energy to reaction coordinate translation propels the reactive system off the IRC, forming vibrationally excited AB product molecules. If the motion had remained on the IRC, with vibrational adiabaticity in moving from the TS to products [130,131], the exit-channel potential energy release would be to product relative translation instead of AB vibration.

IRCs are widely used to describe atomic-level mechanisms for complex, many-atom chemical reactions and only recently has it been recognized that the post-transition state dynamics for these reactions may not follow their IRCs and, instead, may follow dynamical pathways. Non-IRC dynamics were observed in chemical dynamics simulations for cyclopropyl radical ring opening [5], the $OH^- + CH_3F \rightarrow CH_3OH + F^-$ S_N2 reaction [47], the base-mediated decomposition reaction $F^- + CH_3OOH$ [48], 1,2,6-heptatriene rearrangement [133], and the heterolysis rearrangement of protonated pinacolyl alcohol [134]. In recent experiments and chemical dynamics simulation, non-IRC dynamics has been identified for H_2CO and CH_3CHO dissociation via the C–H bond rupture channel [135–137]. The dissociating H-atom crosses a ridge on the PES and 'falls' into the highly exothermic elimination dissociation channel forming H_2 from H_2CO and CH_4 from CH_3CHO. Non-IRC dynamics for such a 'roaming H-atom' mechanism was also observed in earlier studies of H-atom transfer [138,139]. It is noteworthy that non-IRC dynamics has also been identified and explained for the $H + HBr \rightarrow H_2 + Br$ and $O(^3P) + CH_3 \rightarrow H_2 + H + CO$ reactions [140,141]. Non-IRC and non-TS dynamics are prevalent in

high-energy collisions, where the reactive system traverses regions of the PES far above potential minima, IRCs, and TSs [142,143].

Here the non-IRC dynamics found in chemical dynamics simulations of the $OH^- + CH_3F$ and $F^- + CH_3OOH$ reactions are reviewed. These are particularly interesting reactions, since the non-IRC dynamical pathways avoid deep potential energy minima which are connected to the rate-controlling TS via the IRC. This potential energy minimum for the $F^- + CH_3OOH$ reaction is connected to the most exothermic reaction products. The actual dynamics do not form these products, contrary to the IRC prediction.

5.1. $[HO\cdots CH_3\cdots F]^- \rightarrow CH_3OH + F^-$

A direct dynamics simulation at the MP2/6–31 + G* level of theory was used to study the $[HO\cdots CH_3\cdots F]^- \rightarrow CH_3OH + F^-$ post-transition state dynamics for the $HO^- + CH_3F \rightarrow CH_3OH + F^-$ reaction [47]. The MP2/6–31 + G* level of theory provides stationary point energies and structures in good agreement with those obtained with the CCSD(T) theory and large basis sets, including aug-cc-pVTZ. The inclusion of diffuse functions in the basis set is critical for these *ab initio* calculations. The MP2/6–31 + G* classical potential energy changes, in moving from the $[HO\cdots CH_3\cdots F]^-$ central barrier TS to the $HOCH_3\cdots F^-$ intermediate and $CH_3OH + F^-$ products, are 48.5 and 19.9 kcal/mol, respectively. The CCSD(T)/aug-cc-pVTZ values for these energies are 46.9 and 16.6 kcal/mol.

The complete IRC, connecting the central barrier to the reactant and product asymptotic limits, was calculated at the MP2/6–31 + G* level of theory. Energies and geometries along the IRC are shown in Figure 11. The initial IRC, from the central barrier toward products, involves F^- dissociation along an approximate O–C–F collinear axis as

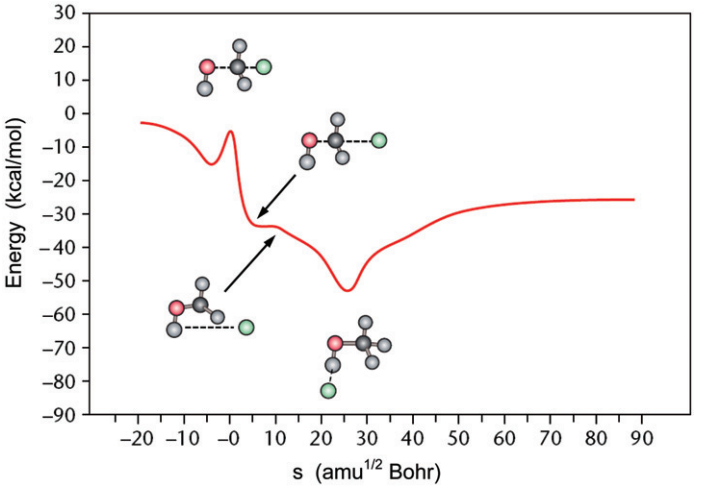

Figure 11. [Colour online] Potential energy along the intrinsic reaction coordinate (IRC) for $OH^- + CH_3F \rightarrow CH_3OH + F^-$; *s* is the distance along the IRC. This figure shows the structures at the potential energy minima and at the saddle point barrier [47].

for a traditional S_N2 reaction, i.e. reaction (13). At s of about 5 atomic mass units ($amu^{1/2}$)-Bohr, the IRC enters a flat region, apparently a remnant of a back-side potential energy minimum, and then starts its descent into the $CH_3OH \cdots F^-$ minimum. Thus, the IRC/RRKM mechanism is an indirect process with the system temporarily trapped in the $CH_3OH \cdots F^-$ minimum.

The direct dynamics trajectories were initiated at the central barrier, with conditions chosen from a 300 K Boltzmann distribution for each of the TS's degrees of freedom, including reaction coordinate translation. Quasiclassical sampling, which includes zero-point energy, was used to choose initial conditions for the trajectories. A trajectory was terminated after 3 ps of motion or when the F^- and CH_3OH product separation exceeded 17 Å.

The trajectories discovered that the system's dynamics, as it moves from the $[HO \cdots CH_3 \cdots F]^-$ central barrier structure to the $CH_3OH + F^-$ products, differs greatly from the IRC/RRKM mechanism. The trajectories have two reaction pathways, one direct and the other indirect, and they are depicted in Figure 12. Neither one is the pathway predicted by the IRC in Figure 11. The vast majority, ~90%, follow a direct reaction pathway with departure of the F^- ion approximately along the $O–C \cdots F^-$ collinear axis. The remaining small fraction of trajectories initially follow the direct pathway, but do not have sufficient $CH_3OH + F^-$ relative translational energy to dissociate and are drawn into the $CH_3OOH \cdots F^-$ minimum and form the IRC/RRKM intermediate.

The origin of the preference for the direct reaction path is seen in Figure 13, in which potential energy is plotted versus the $C \cdots F^-$ distance and $O–C \cdots F^-$ angle. The release of potential energy to the asymmetric $O–C \cdots F^-$ reaction coordinate's stretch motion, as the system moves off the central barrier, tends to propel F^- from CH_3OH, with the $O–C \cdots F^-$ angle maintained at nearly 180°. The PES is rather flat for bending the $O–C \cdots F^-$ angle; there is only a very weak force to pull the reactive system from the direct dissociation reaction path into the $CH_3OH \cdots F^-$ potential energy well, with an $O–C \cdots F^-$ angle of 102.8°. As the system moves off the central barrier, it tends to move directly to products without forming an intermediate trapped in the $CH_3OH \cdots F^-$ potential energy well.

5.2. $F^- + CH_3OOH$

In recent experiments, Kato and coworkers studied the 300 K kinetics of the base-mediated decomposition reaction $F^- + CH_3OOH$ [144]. Much to their surprise, the reaction did not yield the most exothermic products $HF + CH_2(OH)O^-$ and products predicted by the IRC. Instead, they proposed the much higher energy non-IRC products $HF + CH_2O + OH^-$ were formed. The potential energy diagram of the $F^- + CH_3OOH$ reaction, calculated at the B3LYP/6–311G** level of theory [48] is shown in Figure 14. The F^- anion can attack either the H-atom of the OH-group or H-atom of the CH_3-group. The IRC for the latter first leads to a shallow minimum for the $F^- \cdots CH_3OOH$ complex, then TS1 and the deep minimum of the $CH_2(OH)_2 \cdots F^-$ complex. Both the associations $CH_2(OH)_2 + F^-$ and $CH_2(OH)O^- + HF$ are purely attractive, and lead to this deep minimum. F^- attack of the OH^- group forms the $CH_3OOH \cdots F^-$ complex, which can either dissociate to the $HF + CH_3OO^-$ products or isomerize via the low energy TS2 to the $F^- \cdots CH_3OOH$ complex. The experimental proposal is quite intriguing, since the IRC

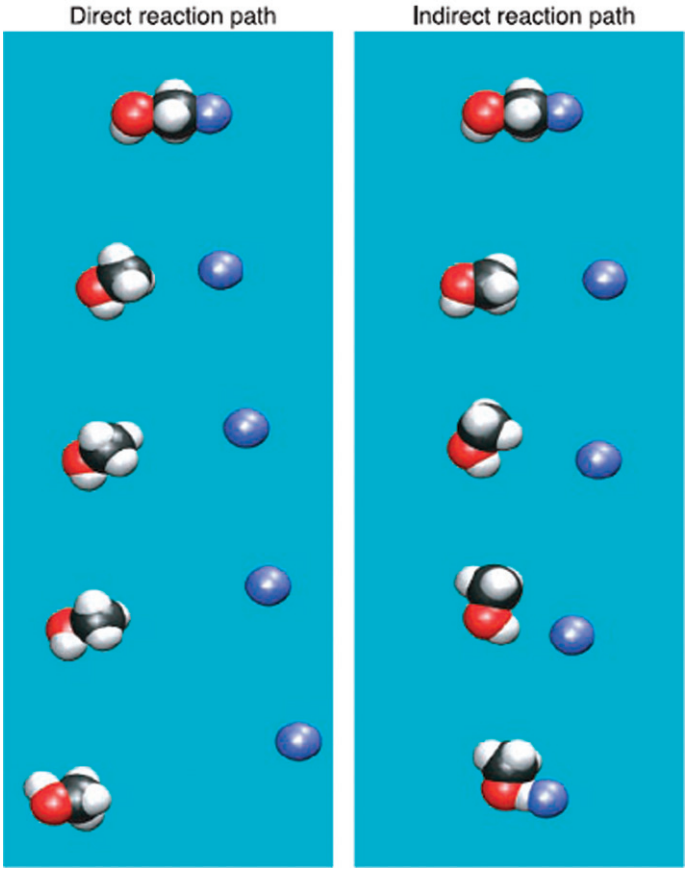

Figure 12. The two pathways for motion from the $[HO\cdots CH_3\cdots F]^-$ central barrier to the $CH_3OH + F^-$ reaction products. Most of the trajectories follow the direct dissociation path. A small amount, roughly 10 percent, form the $CH_3OH\cdots F^-$ hydrogen-bonded intermediate and follow an indirect path [47].

products following TS1 have a much greater exothermicity than do the $HF + CH_2O + OH^-$ products.

The experiments utilized a tandem flowing afterglow-selected ion flow tube (FA-SIFT) mass spectrometer [144]. The measured rate constant is $k = 1.23 \times 10^{-9}\,cm^3/molecule{\cdot}s$, and the major primary product is OH^-. A numerical analysis of the experimental data, suggests that the reaction of F^- with CH_3OOH proceeds mainly via the formation of OH^- (~85%) with an upper bound for direct proton transfer to form CH_3OO^- estimated to be approximately 10% [18].

An $E_{CO}2$ mechanism was proposed for OH^- formation from the experimental results [18]. In this mechanism deprotonation from the α-carbon, by the attacking anion, leads to carbon–oxygen double bond formation with concerted elimination of the anionic leaving group. For the $F^- + CH_3OOH$ reaction, the products of the $E_{CO}2$ mechanism are $HF + CH_2O + OH^-$ Supporting evidence for the $E_{CO}2$ mechanism comes from studying the kinetics of the reverse reaction, $CH_3OO^- + HF$. Measurements with the FA-SIFT

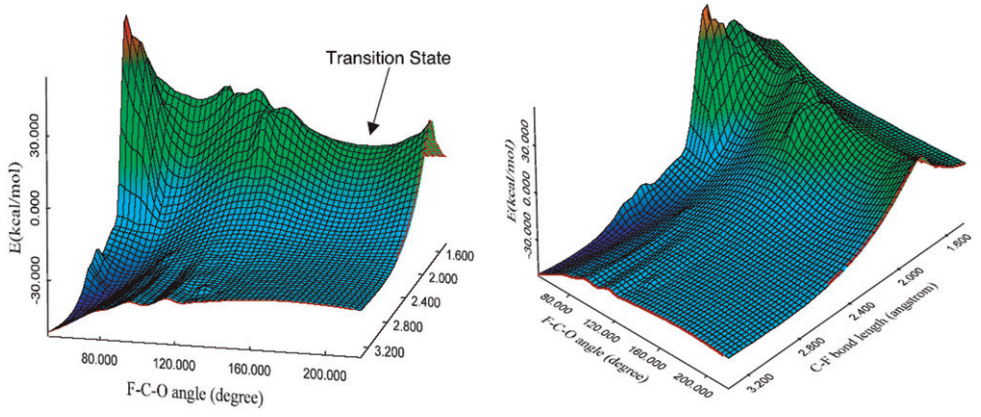

Figure 13. Potential energy contour diagram for $[HO\cdots CH_3\cdots F]^-$ fragmentation as a function of the C–F distance and the O–C $\cdots$ F angle. The remaining coordinates are optimized at each point on the PES [47].

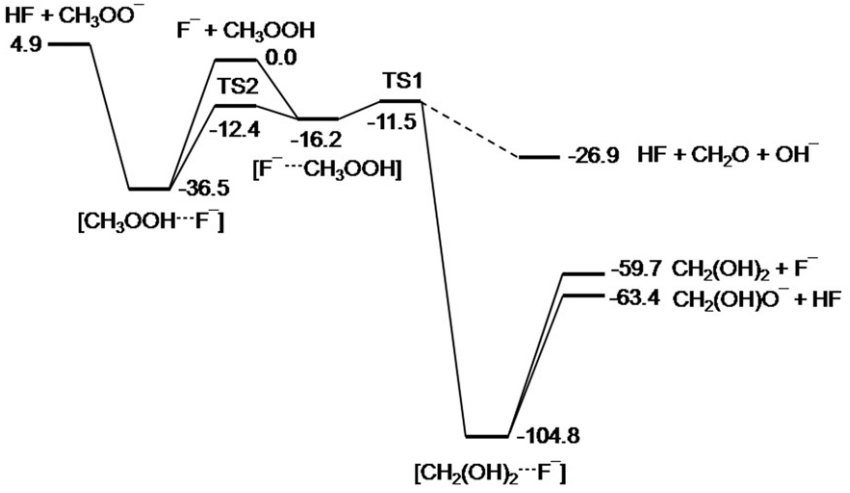

Figure 14. Energy diagram for the $F^- + CH_3OOH$ reaction at the B3LYP/6–311 + G(d,p) level of theory. The energies shown are in kcal/mol and are relative to the $F^- + CH_3OOH$ reactant channel. Zero-point energies are not included. (Reprinted with permission from J. Am. Chem. Soc. **129**, 9976. Copyright 2007. American Chemical Society.)

technique gives a rate constant of $k = 2.43 \times 10^{-9}$ cm^3/molecule·s and identifies, with 81% yield, OH^- as the primary reaction product. The proposal, based in part on *ab initio* calculations (Figure 14), is that the reactants form the $F^- \cdots CH_3OOH$ complex which then dissociates via the $E_{CO}2$ mechanism to form $HF + CH_2O + OH^-$.

To provide an atomic-level understanding of the non-IRC dynamics observed in the experiments a direct dynamics simulation was performed of the $F^- + CH_3OOH$ reaction [48]. In order to study the dynamics for the two pathways in which F^- attacks the H-atoms

Table 7. Products for $F^- + CH_3OOH$ direct dynamics.[a]

Product	Percentage
$HF + CH_3OO^-$	1.5
$CH_3OOH \cdots F^-$	48.5
$HF + CH_2O + OH^-$	22.5
$CH_2(OH)_2 \cdots F^-$	0.0
$F^- + CH_3OOH$	27.5

[a]The trajectories were integrated for 4 ps at the B3LYP/6–311 + G(d,p) level of theory.

of the OH- and CH_3-groups, the trajectories were initiated for the $F^- + CH_3OOH$ reactants with appropriate random initial conditions to model the 300 K experiments. With this sampling, reaction cross-sections and rate constant may be determined from the trajectories. Energies for stationary points on the PES (Figure 14) were calculated at various levels of electronic structure theory. B3LYP/6–311 + G** energies only varied from 0.2 to 3.2 kcal/mol from those of the higher level CBS-QB3 theory. This B3LYP theory is computationally feasible and was used for the simulations.

The trajectories were integrated for 4 ps and the percentages of trajectories for the product channels are listed in Table 7. It is seen that 23% formed $HF + CH_2O + OH^-$ the major product reaction channel observed in the experiment [144], 48% became trapped in the $CH_3OOH \cdots F^-$ potential energy well and formed a reaction intermediate that lasted up to the 4 ps of the trajectory integration, 1.5% formed the $HF + CH_3OO^-$ reaction products, and the remaining trajectories went back to the reactants. None of the trajectories formed the IRC complex. The large fraction of trajectories trapped in the $CH_3OOH \cdots F^-$ potential energy well arises from the high-energy barriers between this complex and the $HF + CH_3OO^-$ products and the $F^- \cdots CH_3OOH$ complex. The long lifetime for $CH_3OOH \cdots F^-$ is consistent with RRKM theory. That none of the trajectories followed the IRC is consistent with the experimental study [144]. The IRC complex and its dissociation products comprise, at most, only 2% of the total experimental product yield. The trajectory total reaction rate constant for $F^- + CH_3OOH$ is $(1.70 \pm 0.7) \times 10^{-9}$ cm^3/molecule·s and in quite good agreement with the experimental value 1.23×10^{-9} cm^3/molecule·s.

Some of $HF + CH_2O + OH^-$ products were formed by trajectories that first formed the $CH_3OOH \cdots F^-$ complex and then formed the products by passing both TS2 and TS1. The PES suggests that the $HF + CH_3OO^-$ product channel should proceed via the $CH_3OOH \cdots F^-$ complex, and since the barrier for this complex to dissociate to $HF + CH_3OO^-$ is 16.4 kcal/mol (see Figure 14) higher than that to dissociate to $HF + CH_2O + OH^-$ it is surprising that the same number of trajectories formed that $HF + CH_3OO^-$ products as first formed $CH_3OOH \cdots F^-$ and then dissociated to $HF + CH_2O + OH^-$. However, visualization of the proton-transfer trajectories to form $HF + CH_3OO^-$ shows that they are direct type events and not mediated by a complex with randomization of its energy.

If the $CH_3OOH \cdots F^-$ complexes remaining, when the trajectories are terminated at 4 ps, are assumed to dissociate statistically as predicted by RRKM, nearly all will form the $HF + CH_2O + OH^-$ products since the barrier is 16.4 kcal/mol lower for this channel as

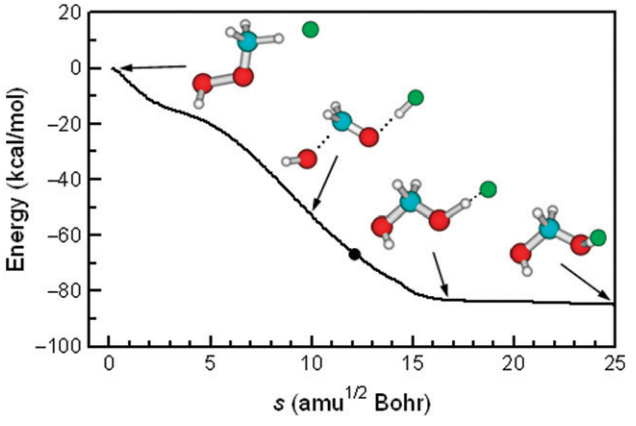

Figure 15. [Colour online] Potential energy along the IRC connecting the transition state TS1 and $CH_2(OH)_2 \cdots F^-$ potential energy minimum. s is the distance along the IRC. (Reprinted with permission from J. Am. Chem. Soc. **129**, 9976. Copyright 2007. American Chemical Society.)

compared to the $HF + CH_3OO^-$ channel. With this assumption, the branching between the $HF + CH_2O + OH^-$ and $HF + CH_3OO^-$ product channels is predicted to be 0.98 ± 0.01 and 0.02 ± 0.01, fractions in qualitative agreement with the experimental results. The experimental estimates of approximately 85% and 10% for these two channels are based on a difficult numerical analysis. The trajectory estimate of only ~2% branching to the $HF + CH_3OO^-$ products is not inconsistent with the experiments.

Energies and geometries for the IRC(s) connecting TS1 with the $CH_2(OH)_2 \cdots F^-$ potential energy minimum are shown in Figure 15. The initial IRC involves H–F and O–H bond formation after rupture of the H–C and O–O bonds to form a tight $HF \cdots CH_2O \cdots HO^-$ complex. For s between 2 and 5 amu$^{1/2}$ Bohr, the IRC has a region with a less negative slope that involves OH^- motion away from CH_2O and rotation of this latter fragment. This rotation allows the migration of OH^- and HF toward the carbon and oxygen atoms of CH_2O, respectively, and a significant energy decrease. At s of about 10 amu$^{1/2}$ Bohr, the IRC shows a complete relocation of the OH^- and HF fragments to form $HO \cdots CH_2O^- \cdots HF$ followed by the formation of $HOCH_2O^- \cdots HF$ and, subsequently, $HOCH_2OH \cdots F^-$ At this point, the IRC enters an extremely shallow region in which the $H \cdots F$ end of the $HOCH_2OH \cdots F^-$ moiety slowly rotates toward OH to finally form the $CH_2(OH)_2 \cdots F^-$ complex, which as illustrated in Figure 14 may dissociate to $HF + CH_2(OH)O^-$ or $CH_2(OH)_2 + F^-$.

The vast majority of the trajectories that formed $HF + CH_2O + OH^-$ followed the pathway depicted in Figure 16. The observation of this pathway provides theoretical evidence for the mechanism proposed by Kato and coworkers [144] for base-mediated heterolytic decomposition of small alkyl hydroperoxides. Figure 16 clearly shows the association of the anion with an α-hydrogen (Figure 16b), crossing of the TS1 barrier (Figure 16c), and rupture of the C–H and O–O bonds (Figure 16d) to form formaldehyde, OH^- and HF (Figure 16e).

Comparison with the IRC, described above, shows the trajectories that form $HF + CH_2O + OH^-$ initially follow the IRC path up to $s \sim 5$ amu$^{1/2}$ Bohr. The dynamics

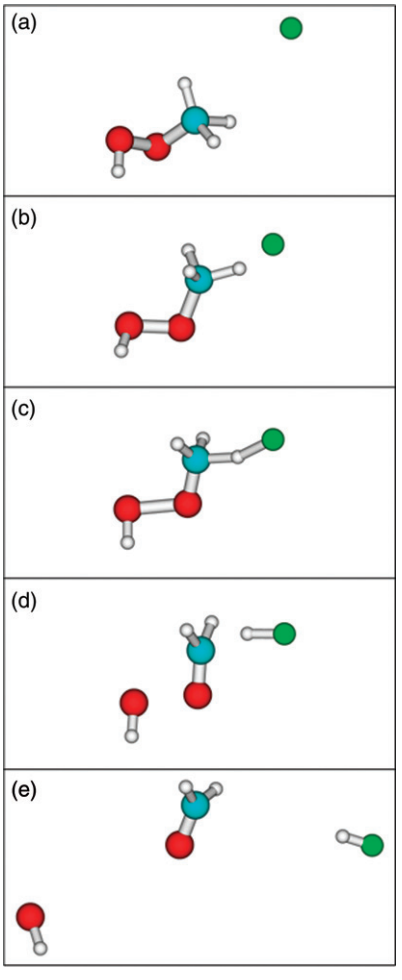

Figure 16. [Colour online] Representative trajectory showing the reaction pathway from the reactants to the major product channel $HF + CH_2O + OH^-$ at (a) 990 fs, (b) 1086 fs, (c) 1108 fs, (d) 1116 fs, and (e) 1290 fs. (Reprinted with permission from J. Am. Chem. Soc. **129**, 9976. Copyright 2007. American Chemical Society.)

of the trajectories show rupture of the H–C and O–O bonds after crossing the TS1 region, formation of a tight $HF \cdots CH_2O \cdots HO^-$ complex, and rotation of the CH_2O fragment. However, the dynamics leads to the separation of OH^- and HF from CH_2O instead of allowing formation of the $HF \cdots CH_2O \cdots HO^-$ IRC structure. The trajectories cease to follow the IRC when the slope of potential energy versus s becomes more negative at $s \sim 5$ amu$^{1/2}$ Bohr.

A two-dimensional contour diagram of the post-transition state potential energy surface, following motion from TS1, is illustrated in Figure 17. Q_1 represents the concerted movement of HF and OH^- away from CH_2O, and Q_2 represents the inplane rotation motion of CH_2O. Also depicted in Figure 17 is the IRC and the motion for a

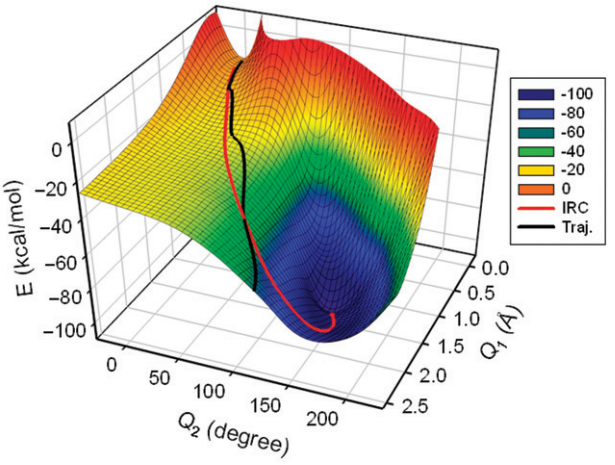

Figure 17. A two-dimensional contour diagram of the post-transition state potential energy surface for TS1. $Q_1 = \Delta r_1 + \Delta r_2$, where r_1 is the FH–C bond length and r_2 is the O–OH bond length. $Q_2 = \Delta\theta_1 + \Delta\theta_2$, where θ_1 is the O–C–O angle and θ_2 is the H–O–C angle; i.e. H is the hydrogen abstracted by F^- and O is the oxygen attached to carbon. Q_1 represents the concerted motion of HF and OH^- away from CH_2O and Q_2 represents rotation of CH_2O. The remaining coordinates were optimized for each Q_1, Q_2 point. Depicted on this contour diagram is the IRC (red line) and a representative trajectory (black line). (Reprinted with permission from J. Am. Chem. Soc. **129**, 9976. Copyright 2007. American Chemical Society.)

representative trajectory. The trajectory 'skirts' the deep potential energy minimum of the $CH_2(OH)_2 \cdots F^-$ IRC complex and has non-IRC dynamics reminiscent of those for the $OH^- + CH_3F \rightarrow CH_3OH + F^-$ reaction [47].

5.3. *Non-IRC post-transition dynamics and time-scales*

The above simulations illustrate that the evaluation of PES features such as well depths, barrier heights, and intrinsic reaction coordinates may be insufficient for determining atomic-level mechanisms for chemical reactions. Instead, it is often necessary to study the actual motion of the atoms on a reactive system's PES. The efficiency of the reactive system to follow the IRC and form reaction intermediates in deep potential energy minima is intimately linked to the hierarchy of time-scales for intramolecular motions and structural transitions on the PES. Inefficient formation of the $CH_3OH \cdots F^-$ reaction intermediate arises from rapid separation of the $CH_3OH + F^-$ products in comparison to the longer time-scale for C–O $\cdots F^-$ bending to form the intermediate.

Following the $F^- \cdots CH_3OOH$ attractive interaction for the $F^- + CH_3OOH$ reaction, the trajectories initially follow the IRC but then leave the IRC forming $HF + CH_2O + OH^-$ instead of going to the $CH_2(OH)_2 \cdots F^-$ deep potential minimum at the bottom of the IRC. The initial motion along the IRC involves rupture of the H–C and O–O bonds forming HF and OH^- weakly attached to CH_2O. The ensuing IRC motion is slow rotation of CH_2O leading to the potential motion. However, this slow rotation cannot compete with the rapid HF and OH^- separations and the IRC is not followed.

Such a hierarchy of time-scales, as found here for the $OH^- + CH_3F$ and $F^- + CH_3OOH$ reactions, has been observed in previous work, where the structural changes of a solvent cage are too slow to allow a reactive system to follow its IRC and access its deep potential energy minimum [145]. A hierarchy of time-scales and inefficient access of deep potential energy minima may be important in enzyme catalysis, where motions associated with the reaction centre may be much faster than those associated with conformational changes and other multiatom motions of the enzyme [146].

The concept that a chemical reaction follows its IRC in moving off a high-energy TS is related to the concept of intramolecular vibrational energy distribution (IVR) [14,15]. To remain on the multi-dimensional IRC, the reaction coordinate translational energy that is acquired by the post-TS potential energy release must be transferred to the reactive system's remaining degrees of freedom. This is expected to become more efficient as the size of the reactive system increases, but there is no certainty this is the case. For the $OH^- + CH_3F$ post-TS dynamics, there is very weak coupling between $CH_3OH + F^-$ relative translation and $O–C\cdots F^-$ bending and other vibrational degrees of freedom, and the reactive system leaves the IRC. For the $F^- + CH_3OOH$ reaction, it is the weak coupling between the HF and OH^- translational motions and other motions, such as the CH_2O rotation, which lead to the non-IRC dynamics.

6. Conclusion

The simulations described above illustrate the detailed information that may be obtained concerning post-transition dynamics of chemical reactions from classical chemical dynamics simulations. If systems are chosen to study for which classical mechanics is applicable and initial conditions are chosen correctly for the trajectories, accurate results are obtained which may be compared with experiment. The simulations provide an atomic-level understanding of the post-transition dynamics and interpretations of the experimental studies. An important finding from the simulations is the often inadequacy of widely used models, such as the intrinsic reaction coordinate and statistical theories, for describing post-transition state dynamics.

The use of direct dynamics simulations allows one to investigate the post-transition state dynamics for a broad-range of chemical systems, and test the predictions of different electronic structure theories and basis sets. As more software packages like VENUS/NWChem [74–76] become available, more simulations like those discussed here will be performed.

Acknowledgements

The research described here was supported by the National Science Foundation under multiple grants and by the Robert A. Welch Foundation under Grant No. D-0005.

References

[1] J. I. Steinfeld, J. S. Francisco and W. L. Hase, *Chemical Kinetics and Dynamics*, 2nd ed. (Princeton Hall, Upper Saddle River, NJ, 1998).

[2] D. G. Truhlar and B. C. Garret, Acc. Chem. Res. **13**, 440 (1992).
[3] B. K. Carpenter, Acc. Chem. Res. **25**, 520 (1992).
[4] W. L. Hase, Acc. Chem. Res. **31**, 659 (1998).
[5] D. J. Mann and W. L. Hase, J. Am. Chem. Soc. **124**, 3208 (2002).
[6] W. L. Hase and K. C. Bhalla, J. Chem. Phys. **75**, 2807 (1981).
[7] W. L. Hase, D. G. Buckowski and K. N. Swamy, J. Phys. Chem. **87**, 2754 (1983).
[8] G. H. Peslherbe and W. L. Hase, J. Chem. Phys. **104**, 7882 (1996).
[9] G. Vayner, S. V. Addepalli, K. Song, *et al*., J. Chem. Phys. **125**, 014317 (2006).
[10] T. Baer and W. L. Hase, *Unimolecular Reaction Dynamics. Theory and Experiments* (Oxford University Press, New York, 1996).
[11] K. Fukui, J. Phys. Chem. **74**, 4161 (1970).
[12] J. Chandrasekhar, S. F. Smith and W. L. Jorgensen, J. Am. Chem. Soc. **106**, 3049 (1984).
[13] J. Gao and D. G. Truhlar, Annu. Rev. Phys. Chem. **53**, 467 (2002).
[14] W. L. Hase, J. Phys. Chem. **90**, 365 (1986).
[15] T. Uzer, Phys. Rep. **199**, 73 (1991).
[16] W. J. Chesnavich and M. T. Bowers, in *Gas Phase Ion Chemistry*, edited by M. T. Bowers (Academic, New York, 1979), Vol. 1, p. 119.
[17] M. Quack and J. Troe, Ber. Bunsenges. Phys. Chem. **79**, 470 (1975).
[18] S. J. Klippenstein and R. A. Marcus, J. Chem. Phys. **91**, 2280 (1989).
[19] K. Bolton, W. L. Hase and G. H. Peslherbe, in *Modern Methods for Mutidimentional Dynamics Computations in Chemistry*, edited by D. L. Tompson (World Scientific, Singapore, 1998), p. 143.
[20] W. L. Hase, G. Mrowka, R. J. Brudzynski, *et al*., J. Chem. Phys. **69**, 3548 (1978).
[21] S. R. Vande Linde and W. L. Hase, J. Phys. Chem. **94**, 2778 (1990).
[22] U. Burkert and N. L. Allinger, *Molecular Mechanics* (American Chemical Society, Washington D. C., 1982).
[23] R. D. Levine and R. B. Bernstein, *Molecular Reaction Dynamics and Chemical Reactivity* (Oxford University Press, New York, 1987).
[24] L. Sun and W. L. Hase, in *Review in Computational Chemistry*, edited by K. Lipkowitz, R. Larter, and T. R. Cundari (Willey, New York, 2003), Vol. 19, p. 79.
[25] W. L. Hase, K. Song and M. S. Gordon, Comput. Sci. Eng. **5**, 36 (2003).
[26] I. S. Y. Wang and M. Karplus, J. Am. Chem. Soc. **95**, 8160 (1973).
[27] C. LeForestier, J. Chem. Phys. **68**, 4406 (1978).
[28] H. Wang, G. H. Peslherbe and W. L. Hase, J. Am Chem. Soc. **116**, 9644 (1994).
[29] L. Sun and W. L. Hase, J. Chem. Phys. **121**, 8831 (2004).
[30] E. Dong, D. W. Sester, W. L. Hase, *et al*., J. Phys. Chem. A. **110**, 1484 (2006).
[31] L. Sun, K. Park, K. Song, *et al*., J. Chem. Phys. **124**, 064313 (2006).
[32] C. Doubleday Jr, K. Bolton and W. L. Hase, J. Am. Chem. Soc. **119**, 5251 (1997).
[33] D. A. Hrovat, S. Fang, W. T. Borden, *et al*., J. Am. Chem. Soc. **119**, 5253 (1997).
[34] K. Bolton, W. L. Hase and C. Doubleday Jr, Ber. Bunsenges. Phys. Chem. **101**, 414 (1997).
[35] C. Doubleday Jr, K. Bolton and W. L. Hase, J. Phys. Chem. A **102**, 3648 (1998).
[36] S. R. Vande Linde and W. L. Hase, J. Am. Chem. Soc. **111**, 2349 (1989).
[37] S. R. Vande Linde and W. L. Hase, J. Chem. Phys. **93**, 7962 (1990).
[38] S. R. Vande Linde and W. L. Hase, J. Phys. Chem. **94**, 6148 (1990).
[39] Y. J. Cho, S. R. Vande Linde, L. Zhu, *et al*., J. Chem. Phys. **96**, 8275 (1992).
[40] W. L. Hase and Y. J. Cho, J. Chem. Phys. **98**, 8626 (1993).
[41] W. L. Hase, Science **266**, 998 (1994).
[42] G. H. Peslherbe, H. Wang and W. L. Hase, J. Chem. Phys. **102**, 5626 (1995).
[43] D. J. Mann and W. L. Hase, J. Phys. Chem. A **102**, 6208 (1998).
[44] G. Li and W. L. Hase, J. Am. Chem. Soc. **121**, 7124 (1999).
[45] L. Sun, W. L. Hase and K. Song, J. Am. Chem. Soc. **123**, 5753 (2001).

[46] S. Cheon, K. Song and W. L. Hase, THEOCHEM: J. Molec. Struc. **771**, 27 (2006).
[47] L. Sun, K. Song and W. L. Hase, Science **296**, 875 (2002).
[48] J. G. Lopez, G. Vayner, U. Lourderaj, *et al*., J. Am. Chem. Soc. **129**, 9976 (2007).
[49] W. L. Hase, in *Encyclopedia of Computational Chemistry*, edited by N. L. Allinger (Wiley, New York, 1998), Vol. 1, pp. 399–402.
[50] G. H. Peslherbe, H. Wang and W. L. Hase, Adv. Chem. Phys. **105**, 171 (1999).
[51] R. Car and M. Parrinello, Phys. Rev. Lett. **55**, 2471 (1985).
[52] J. M. Herbert and M. Head-Gordon, J. Chem. Phys. **121**, 11542 (2004).
[53] D. L. Bunker, Meth. Comput. Phys. **10**, 287 (1971).
[54] P. Pulay and G. Fogarasi, Chem. Phys. Lett. **386**, 272 (2004).
[55] A. M. N. Niklasson, C. J. Tymczak and M. Challacombe., Phys. Rev. Lett. **97**, 123001 (2006).
[56] J. M. Herbert and M. Head-Gordon, Phys. Chem. Chem. Phys. **7**, 3269 (2005).
[57] S. K. Gray, D. W. Noid and B. G. Sumpter, J. Chem. Phys. **101**, 4062 (1994).
[58] R. D. Skeel, G. Zhang and T. Schlick, SIAM. J. Sci. Compt. **18**, 203 (1997).
[59] U. Lourderaj, K. Song, T. L. Windus, *et al*., J. Chem. Phys. **126**, 044105 (2007).
[60] V. I. Arnold, *Mathematical Methods of Chemical Mechanics* (Springer-Verlag, New York, 1978).
[61] L. Verlet, Phys. Rev. **159**, 98 (1967).
[62] T. Schlick, *Molecular Modeling and Simulation* (Springer, New York, 2000).
[63] Ch. Schlier and A. Seiter, J. Phys. Chem. A **102**, 9399 (1998).
[64] Ch. Schlier and A. Seiter, Comp. Phys. Commun. **130**, 176 (2000).
[65] T. Helgaker, E. Uggerud and H. J. Jensen, Chem. Phys. Lett. **173**, 145 (1990).
[66] J. M. Millam, V. Bakken, W. Chen, *et al*., J. Chem. Phys. **111**, 3800 (1999).
[67] J. M. Bofill, J. Comput. Chem. **15**, 1 (1994).
[68] V. Bakken, J. M. Millam and H. B. Schlegel, J. Chem. Phys **111**, 8773 (1999).
[69] W. H. Miller, N. C. Handy and J. E. Adams, J. Chem. Phys. **72**, 99 (1980).
[70] S. Chapman and D. L. Bunker, J. Chem. Phys. **62**, 2890 (1975).
[71] T. Yan and W. L. Hase, J. Phys. Chem. A **105**, 2617 (2001).
[72] K. Bolton, H. B. Schlegel, W. L. Hase, *et al*., Phys. Chem. Chem. Phys. **1**, 999 (1999).
[73] K. C. Thompson, M. J. T. Jordon and M. A. Collins, J. Chem. Phys **108**, 564 (1998).
[74] W. L. Hase, R. J. Duchovic, S. Hu, *et al*., Quantum Chemistry Program Exchange (QCPE) Bulletin **16**, 671 (1997).
[75] E. Aprà, *et al*., *NWCHEM, a Computational Chemistry Package for Parallel Computers*, version 4.7 (Pacific Northwest Laboratory, Richland, WA 99352, 2005).
[76] R. A. Kendall, E. Aprà, D. E. Bernholdt, *et al*., Comput. Phys. Commun. **128**, 260 (2000).
[77] *Advances in Classical Trajectory Methods, Vol. 3, Comparisons of Classical and Quantum Dynamics*, edited by W. L. Hase (JAI Press, London, 1998).
[78] S. Yu. Grebenshchikov, R. Schinke and W. L. Hase, in *Comprehensive Chemical Kinetics*, edited by N. J. B. Green (Elsevier, Amsterdam, 2003), Vol. 39.
[79] K. N. Swamy and W. L. Hase, J. Phys. Chem. **87**, 4715 (1983).
[80] D.-h. Lu and W. L. Hase, J. Chem. Phys. **89**, 6723 (1988).
[81] C. Doubleday Jr, K. Bolton, G. H. Peslherbe, *et al*., J. Am. Chem. Soc. **118**, 9922 (1996).
[82] T. Beyer and D. R. Swinehart, Commun. ACM **16**, 379 (1973).
[83] L. Zhu and W. L. Hase, Chem. Phys. Lett. **175**, 117 (1990).
[84] E. E. Aubanel, D. M. Wardlaw, L. Zhu, *et al*., Int. Rev. Phys. Chem. **10**, 249 (1991).
[85] L. Zhu, W. Chen, W. L. Hase, *et al*., J. Phys. Chem. **97**, 311 (1993).
[86] D. L. Bunker and W. L. Hase, J. Chem. Phys. **59**, 4621 (1973).
[87] W. H. Miller, W. L. Hase and C. L. Darling, J. Chem. Phys. **91**, 2863 (1989).
[88] J. C. Tully and R. K. Preston, J. Chem. Phys. **55**, 562 (1971).
[89] R. Schinke, *Photodissociation Dynamics* (Cambridge, Iniversity Press, Cambridge, 1993).
[90] A. Untch, R. Schinke, R. Cotting, *et al*., J. Chem. Phys. **99**, 9553 (1993).
[91] W. F. Polik, D. R. Guyer, W. H. Miller, *et al*., J. Chem. Phys. **92**, 3471 (1990).

[92] W. L. Hase, S.-W. Cho, D.-h. Lu, *et al.*, Chem. Phys. **139**, 1 (1989).
[93] B. A. Waite and W. H. Miller, J. Chem. Phys. **73**, 3713 (1980).
[94] A. J. Dobbyn, M. Stumpf, H.-M. Keller, *et al.*, J. Chem. Phys. **104**, 8357 (1996).
[95] C. Li, P. Ross, J. E. Szulejko, *et al.*, J. Am. Chem. Soc. **118**, 9360 (1996).
[96] D. S. Tonner and T. B. McMahon., J. Am. Chem. Soc. **122**, 8783 (2000).
[97] W. L. Hase and D. G. Buckowski, J. Comput. Chem. **3**, 335 (1982).
[98] W. Chen, W. L. Hase and H. B. Schlegel, Chem. Phys. Lett. **228**, 436 (1994).
[99] A. A. Viggiano, R. A. Morris, J. S. Paschkewitz, *et al.*, J. Am. Chem. Soc. **114**, 10477 (1992).
[100] H. Wang and W. L. Hase, J. Am. Chem. Soc. **117**, 9347 (1995).
[101] S. L. Craig and J. I. Brauman, J. Phys. Chem. A **101**, 4745 (1997).
[102] S. L. Graul and M. T. Bowers, J. Am. Chem. Soc. **113**, 9696 (1991).
[103] S. Graul and M. T. Bowers, J. Am. Chem. Soc. **116**, 3875 (1994).
[104] Y. Wang, W. L. Hase and H. Wang, J. Chem. Phys. **118**, 2688 (2003).
[105] L. A. Angel and K. M. Ervin, J. Am. Chem. Soc. **125**, 1014 (2003).
[106] H. W. Chang, D. W. Setser and M. J. Perona, J. Phys. Chem. **75**, 2070 (1971).
[107] H. W. Chang, N. L. Craig and D. W. Setser, J. Phys. Chem. **76**, 954 (1972).
[108] E. Arunan, S. J. Wategaonkar and D. W. Setser, J. Phys. Chem. **95**, 1539 (1991).
[109] C. R. Quick Jr and C. Wittig, J. Chem. Phys. **72**, 1694 (1980).
[110] E. Zamir and R. D. Levine, Chem. Phys. **52**, 253 (1980).
[111] B. E. Holmes and D. W. Setser, J. Phys. Chem. **82**, 2450 (1978).
[112] A. S. Sudbo, P. A. Schultz, Y. R. Shen, *et al.*, J. Chem. Phys. **69**, 2312 (1978).
[113] C. F. Giese and W. R. Gentry, Phys. Rev. A **10**, 2156 (1974).
[114] Reference 89, p. 124.
[115] A. L. Kaledin and W. H. Miller, J. Chem. Phys. **118**, 7174 (2003).
[116] M. J. Berry, J. Chem. Phys. **61**, 3114 (1974).
[117] D. J. Zvijac and J. C. Light, Chem. Phys. **21**, 411 (1977).
[118] G. C. Schatz and J. Ross, J. Chem. Phys. **66**, 1021 (1977).
[119] J. A. Berson, L. D. Pederson and B. K. Carpenter, J. Am. Chem. Soc. **98**, 122 (1976).
[120] J. E. Baldwin, S. J. Cianciosi, D. A. Glenar, *et al.*, J. Am. Chem. Soc. **114**, 9408 (1992).
[121] S. W. Benson, J. Chem. Phys. **34**, 521 (1961).
[122] F. T. Smith, J. Chem. Phys. **29**, 235 (1958).
[123] R. Hoffmann, J. Am. Chem. Soc. **90**, 1475 (1968).
[124] C. Doubleday Jr, K. Bolton, G. H. Peslherbe, *et al.*, J. Am. Chem. Soc. **118**, 9922 (1996).
[125] A. Gonzalez-Lafont, T. N. Truong and D. G. Truhlar, J. Phys. Chem. **95**, 4618 (1991).
[126] C. Doubleday, G. Li and W. L. Hase, Phys. Chem. Chem. Phys. **4**, 304 (2002).
[127] D. A. Hrovat, S. Fang, W. T. Borden, *et al.*, J. Am. Chem. Soc. **119**, 5253 (1997).
[128] W. L. Hase, S. L. Mondro, R. J. Duchovic, *et al.*, J. Am. Chem. Soc. **109**, 2916 (1987).
[129] W. H. Miller, N. C. Handy and J. E. Adams, J. Chem. Phys. **72**, 99 (1980).
[130] R. A. Marcus, J. Chem. Phys. **45**, 4493 (1966).
[131] M. Quack and J. Troe, Ber. Bunsenges. Phys. Chem. **78**, 240 (1974).
[132] J. C. Polanyi, Acc. Chem. Res. **5**, 161 (1972).
[133] S. L. Debbert, B. K. Carpenter, D. A. Hrovat, *et al.*, J. Am. Chem. Soc. **124**, 7896 (2002).
[134] S. C. Ammal, H. Yamataka, M. Aida, *et al.*, Science **299**, 1555 (2003).
[135] D. Townsend, S. A. Lajankar, S. K. Lee, *et al.*, Science **306**, 1158 (2004).
[136] S. A. Lahankar, S. D. Chambreau, D. Townsend, *et al.*, J. Chem. Phys. **125**, 044303 (2006).
[137] P. L. Houston and S. H. Kable, Proc. Natl. Acad. Sci. U. S. A. **103**, 16079 (2006).
[138] M. A. ter Horst, G. C. Schatz and L. B. Harding, J. Chem. Phys. **105**, 558 (1996).
[139] D. Troya, M. González, G. Wu, *et al.*, J. Phys. Chem. A **105**, 2285 (2001).
[140] A. E. Pomerantz, J. P. Camden, A. S. Chiou, *et al.*, J. Am. Chem. Soc. **127**, 16368 (2005).
[141] T. P. Marcy, R. R. Díaz, D. Heard, *et al.*, J. Phys. Chem. A **105**, 8361 (2001).

[142] S. O. Meroueh, Y. Wang and W. L. Hase, J. Phys. Chem. A **106**, 9983 (2002).
[143] T. Yan, C. Doubleday and W. L. Hase, J. Phys. Chem. A **108**, 9863 (2004).
[144] S. J. Blanksby, G. B. Ellison, V. M. Bierbaum, *et al.*, J. Am. Chem. Soc. **124**, 3196 (2002).
[145] X. Hu and W. L. Hase, J. Phys. Chem. **96**, 7535 (1992).
[146] A. Fersht, *Enzyme Structures and Mechanism*, 2nd ed. (Freeman, New York, 1985).